A re-evaluation of mixed-mode cohesive zone modeling based on strength concepts instead of traction laws*

John A. Nairn

Wood Science and Engineering, Oregon State University, Corvallis, OR 97330, USA
Email: John.Nairn@oregonstate.edu

Yamina E. Aimene

University of West Indies – Ecofog, Pôle Martinique, Schoelcher 97233, France
Email: Yamina.Aimene@univ-antilles.fr

Abstract

New methods for implementing cohesive zones in computational mechanics were derived by re-interpreting cohesive-zone "traction laws" as "strength models" and using concepts from damage mechanics. When applied to pure mode I or mode II loading, this approach is identical to prior methods. But, when applied to mixed-mode loading, it defines a new approach called strength cohesive zone modeling (or "strength CZM"). Compared to previous methods, strength CZM provides improved modeling for problems with changing mode mixity, allows independent selection of normal and tangential strength models, and reveals limitations in any method based on effective displacements. New modeling shows that mode mixity, which changes during crack growth, depends on cohesive zone properties and on which end of the cohesive process zone is interpreted as the crack tip. These observations suggest many prior experimental results need reanalysis. By considering a range of independent strength models, strength CZM predicts that all G_I-G_{II} failure envelopes are convex. Precracking steps recommended in delamination testing protocols are considered. Strength CZM can realistically model precracking while prior methods generate unrealistic predictions.

Keywords: A. Cohesive Zones, B. Material Point Method, C. Mixed-Mode Fracture, D. Damage Mechanics, E. Process Zones

1. Introduction

Composite materials, adhesive bonds, and stratified media (*e.g.*, sedimentary rock) often fail by crack propagation along weak interfaces within the materials. Such failure processes can be studied using fracture tests for composite delaminations [1] or adhesive failures [2]. While

Engineering Fracture Mechanics, in press, 18 March 2021 (author-prepared preprint)

experiments focus on constant mode mixity (pure mode I or II or fixed mode I/II ratio [3]), real-world failures may involve variations in mode mixity. A common approach to modeling such failures is to introduce cohesive zones along the interface. We have re-evaluated numerical cohesive zone modeling (CZM) methods with the goal of deriving improved capabilities for modeling failures when mode mixity varies during loading.

CZM began when Dugdale [4] imagined a plastic line zone ahead of a crack tip. The tractions within the zone were set equal to the material's yield strength. Dugdale's concept was extended to allow zone traction to depend on crack opening displacement and used to gain insights into elastic-plastic fracture mechanics [5, 6]. These simplified plasticity models did not consider unloading and are therefore limited to monotonically increasing loads [6]. More recent CZM has modeled weak interfaces as an elastic zone with damage. During loading, zone tractions initially increase elastically until damage starts and then evolve eventually decaying to zero at a critical crack opening displacement. Because such zones are elastic, if loading is interrupted, zone tractions should decrease back to the origin with a reduced slope compared to the initial elastic stiffness. If loading resumes, tractions increase with the same reduced stiffness until returning to conditions that cause new damage evolution.

Elastic/damage cohesive zones can be interpreted as modeling a crack-tip process zone, consisting of some remaining elastic material along with development of microcracks, voids, fiber bridging, or other forms of damage. Modeling methods for elastic/damage cohesive zones are clarified by replacing the traditional concept of "traction laws" with the concept of "strength models," that define residual strength as a function of an evolving damage state. This approach is closer to continuum damage mechanics [7–10] than to elastic-plastic Dugdale zones and is the one used in this paper.

CZM during unidirectional (normal or tangential) loading with unloading is straightforward and most published methods are the same. When deformations are mixed mode, however, modeling options diverge [11]. One common approach is characterized as "decoupled" damage. It treats damage by normal and tangential opening separately as if they are damaging under unidirectional loading [12, 13]. This approach has two drawbacks. First, it does not depend on loading history. Imagine loading a zone in tension and inducing some damage. If this zone was unloaded and then reloaded in shear, it would act as a virgin material with no damage. Such a response is likely unrealistic. Second, because mode I and mode II components evolve independently, failure modeling must impose some mixed-mode failure criterion [12, 13]. A drawback of imposing failure criteria is that they predict mixed-mode failure before normal and tangential tractions reach zero. Such sudden traction drops are "impact" events that may cause numerical issues and may be a poor model for failure.

Other CZM methods can be characterized as "coupled" damage, but differ by methods used to couple normal and tangential deformations. Several models are based on tracking evolution of an *effective* displacement such as [6]

$$u_{eff} = \sqrt{\left(\frac{u_n}{u_n^{(c)}}\right)^2 + \left(\frac{u_t}{u_t^{(c)}}\right)^2} \tag{1}$$

where u_n and u_t are normal and tangential displacements and $u_n^{(c)}$ and $u_t^{(c)}$ are critical dis-

placements for failure in normal and tangential directions. This approach was first used for plasticity cohesive zones [6]. Examples of elastic/damage cohesive zones based on effective displacement are found in Camacho and Ortiz [14], Camanho and Dàvila [15], and Högberg [16]. An advantage of effective displacement approaches is that mixed-mode modeling becomes a simple extension of unidirectional modeling. A drawback, whether stated or not, is that it limits choices for normal and tangential strength models.

Another option for coupling normal and tangential damage is to include it within the "traction laws." For example, Needleman and Xu [17, 18] propose potential energies depending on normal and tangential separations that are differentiated to get normal and tangential tractions. This approach can handle coupling for monotonically increasing displacements at constant mode mixity. Most potential-based implementations, however, do not cover methods needed to handle unloading or changes in mode mixity [11].

This paper analyzes mixed-mode CZM using damage mechanics and strength models resulting in a new approach labeled "strength CZM" with these properties:

- Initial elastic loading as well as subsequent elastic unloading and reloading is always a superposition of normal and tangential tractions. The normal and tangential stiffnesses vary with damage state.

- The concept of "traction laws" is replaced by the concept of "strength models." Strength CZM allows independent selection of normal and tangential strength models. These models are combined to construct a mixed-mode failure surface (which is one step in coupling). Damage evolves whenever tractions reach the current failure surface.

- The zone's damage state is described by four evolving damage state variables. These damage variables are then coupled into a single damage parameter by requiring normal and tangential tractions to simultaneously reach zero at decohesion.

Compared to a decoupled approach, strength CZM does not impose a mixed-mode failure criterion. Rather, mixed-mode failure envelopes are modeling outputs that depend on choice of normal and tangential strength models. Compared to effective displacement methods, strength CZM can use independent strength models. Effective displacement methods, as shown below, are only valid when normal and tangential strength models are scaled copies of each other. Compared to potential-based methods, strength CZM methods could be used to supplement their coupled tractions with new methods for loading and unloading and changes in mode mixity. The wisdom of adopting this approach, however, is questioned.

Modeling with cohesive zones along a crack path leads to a process zone with a "zone tip" at its leading edge and a "debond tip" at its trailing edge [19]. The "Results and Discussion" section uses strength CZM to examine mixed-mode partitioning in the presence of process zones and defines two types of R curves for finding toughness as a function of crack growth — one based on zone tip growth and one based on debond tip crack growth. Calculations of G_I as a function of G_{II} to cause debonding showed that strength CZM always predicts such mixed-mode failure curves to be convex. Many mixed-mode experiments are consistent with this prediction. Prior reports of concave G_I–G_{II} curves may have been caused by invalid mode

I/mode II partitioning methods that could be corrected by reanalysis using strength CZM. Finally, a common technique in fracture testing is precracking [20], but its use can cause unexpected results when process zones are present. Strength CZM can potentially evaluate those effects better than prior methods.

Nomenclature

Symbol(s)	Description
Γ_I, Γ_{II}	Cumulative mode I or II released energy
D, D_n, D_t	Generic, normal, or tangential dimensionless damage parameter
δ, δ_n, δ_t	Generic, normal, or tangential damage state variable
ζ	An alternate damage state variable
$F(u)$	Zone traction *vs*. displacement under monotonic loading
G_{tot}, G_I, G_{II}	Total, mode I, or mode II energy release rate
G_c, G_{Ic}, G_{IIc}	Total, mode I, or mode II critical energy release rate
J, J_I, J_{II}	Total, mode I, or mode II J integral
k, k_n, k_t	Generic, normal, or tangential initial elastic stiffness
k_{eff}	Effective elastic stiffness
Π	Potential Energy
r_e, r_c	Ratio of normal to tangential elastic or critical displacements
r	The ratio r_e/r_c
R	Toughness as a function of crack growth
$\mathbb{R}(\delta)$, $\mathbb{R}_n(\delta_n)$, $\mathbb{R}_t(\delta_t)$	Generic, normal, or tangential D-δ evolution ratio
$S(\delta)$, $S_n(\delta_n)$, $S_t(\delta_t)$	Generic, normal, or tangential strength model
σ_c, σ_{nc}, σ_{tc}	Generic, normal, or tangential cohesive stress
T, T_n, T_t	Generic, normal, or tangential traction
θ, θ'	Mode mixity angles
u, u_n, u_t	Generic, normal, or tangential displacement
$u^{(c)}$, $u_n^{(c)}$, $u_t^{(c)}$	Generic, normal, or tangential critical displacement
$u^{(e)}$, $u_n^{(e)}$, $u_t^{(e)}$	Generic, normal, or tangential elastic-limit displacement
u_{eff}	Effective displacement
$u_{elastic}$	Displacement due to elastic loading
u_{damage}	Displacement due to damage (microcracks, voids, *etc*.)
U	Strain energy
$\varphi(\delta)$, $\varphi_n(\delta_n)$, $\varphi_t(\delta_t)$	Generic, normal, or tangential dissipation rate function
W	Work
Ω, Ω_I, Ω_{II}	Total, mode I, or mode II dissipated energy
ω, λ, λ_ω, $\lambda_p(\theta')$, $H(\lambda)$	Terms used in Högberg approach

2. Strength Cohesive Zone Modeling

Strength CZM is first derived in 1D or for unidirectional normal or tangential loading. While the results are analogous to prior, accepted 1D CZM, this derivation includes concepts used later for mixed-mode analysis. Figure 1 shows a possible 1D cohesive zone traction, $F(u)$,

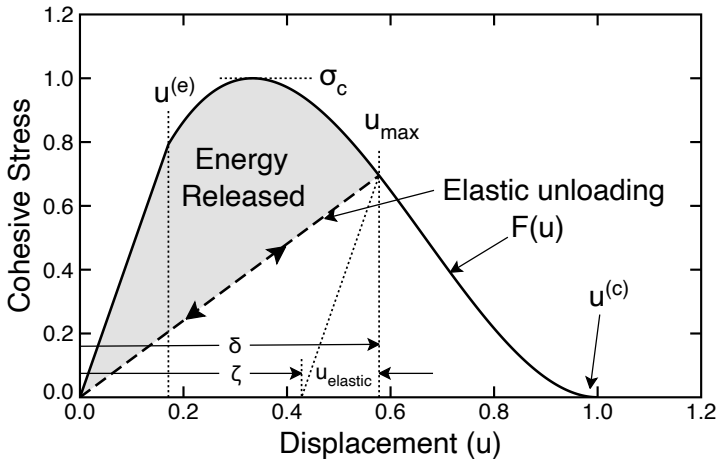

Figure 1: A sample traction response of a cohesive zone in unidirectional loading. The dashed line shows traction during unloading and reloading at a constant state of damage. The shaded area between $F(u)$ and the dashed unloading line is total energy dissipated by loading up to displacement u.

during monotonically increasing loads as a function of zone displacement, u. This example has an initial linear-elastic region with stiffness k ending at $u = u^{(e)}$. After $u^{(e)}$, the zone starts to evolve damage; the traction becomes non-linear, reaches a peak stress, σ_c, and then decays to zero at critical displacement $u = u^{(c)}$. Traction relations like Fig. 1 are labeled as the zone's "traction law," but that terminology is misleading. For example, if unloading occurs, the traction unloads elastically (with no energy dissipation) to the origin and then reloads along the same elastic path until it returns to $F(u)$. In other words, $F(u)$ defines an *envelope* of possible tractions as a function of u. It is labeled here as the zone's "cohesive law."

2.1. Unidirectional Modeling

In 1D strength CZM, $F(u)$ has to be supplemented with a "strength model," $S(\delta)$, that describes changes in zone strength as a function of a damage state variable, δ, defined in 1D by $\delta = \max(u)$. Because strength does not change during initial elastic loading, we initialize $\delta_0 = u^{(e)}$ for the state with no damage. Thereafter, a unidirectional strength is easily derived as $S(\delta) = F(\delta)$ for $u^{(e)} \le \delta \le u^{(c)}$. The strength for $\delta < u^{(e)}$ is not needed. The differences between cohesive law $F(u)$ and strength model $S(\delta)$ in 1D are mostly semantics, but mentioned here because their differences are important in mixed-mode analysis.

By a strength model interpretation, cohesive zone tractions are defined by a line from the origin to the current strength:

$$T(u) = \frac{S(\delta)}{\delta} u = k_{eff} u \qquad \text{where} \qquad k_{eff} = \frac{S(\delta)}{\delta} \tag{2}$$

By initializing $\delta_0 = u^{(e)}$, this traction applies during initial elastic loading as well. At a constant damage state, the zone material is linear elastic (with effective stiffness k_{eff}) and has strain

energy, U, defined by integrating current tractions:

$$U(u,\delta) = \int_0^u T(u)\,du = \frac{1}{2}\frac{S(\delta)}{\delta}u^2$$

Although δ is sufficient for 1D analysis, we define two alternate damage variables. First, divide total cohesive zone displacement into $u = u_{elastic} + u_{damage}$, where $u_{elastic}$ is displacement within elastic material in the cohesive zone and u_{damage} is displacement due to damage (*e.g.*, opening of microcracks or voids). Next, assume that only elastic displacements induce tractions or $T = ku_{elastic} = k(u - u_{damage})$ where k is the undamaged zone's stiffness (note that this analysis accommodates $F(u)$ with no initial linear elastic regime by defining $k = \lim_{\delta\to 0} k_{eff} = S'(0)$). Two alternate damage state variables are:

$$D = \frac{u_{damage}}{u} \quad \text{and} \quad \zeta = \max(u_{damage})$$

The first, D, is a dimensionless damage parameter that evolves from 0 to 1 at failure [7]. Substituting into the traction equation gives

$$T = k(u - u_{damage}) = k(1-D)u = k_{eff}u \qquad \text{where} \qquad \mathrm{k_{eff}} = \mathrm{k(1-D)} \tag{3}$$

Comparing Eq. (3) to Eq. (2) gives a D–δ relation and a new form for strain energy:

$$D = 1 - \frac{S(\delta)}{k\delta} \qquad \text{and} \qquad U(u,D) = \frac{1}{2}k(1-D)u^2 = (1-D)U(u,0) \tag{4}$$

where $U(u,0) = ku^2/2$ is strain energy in the absence of damage. δ and ζ for a given u_{max} are illustrated in Fig. 1; ζ is found by subtracting $u_{elastic}$, defined by back extrapolating along initial stiffness to zero traction, from δ:

$$\zeta = \delta - u_{elastic} = \delta - \frac{S(\delta)}{k} = D\delta \tag{5}$$

Note that ζ evolves from 0 to $u^{(c)}$ at failure, δ evolves from $u^{(e)}$ to $u^{(c)}$, and their ratio is D.

1D CZM can proceed using any one of these damage variables. For these three approaches to match, however, their strength models must be consistent. If we start with strength model using δ as $S(\delta)$, strength models using D or ζ would be $S(D) = S(D^{-1}(\delta))$ and $S(\zeta) = S(\zeta^{-1}(\delta))$, where these inverse functions are found by solving Eq. (4) or (5) for δ. For example, using a sawtooth cohesive law (see Appendix C) for $S(\delta)$ results in strength models in terms of each damage variable as:

$$S(\delta) = \sigma_c\frac{u^{(c)} - \delta}{u^{(c)} - u^{(e)}}, \quad S(D) = \sigma_c\frac{(1-D)u^{(c)}}{u^{(c)} - D(u^{(c)} - u^{(e)})}, \quad \text{and} \quad S(\zeta) = \sigma_c\left(1 - \frac{\zeta}{u^{(c)}}\right)$$

Whether δ, D, or ζ are preferred, is likely irrelevant. To facilitate comparison to most prior CZM, this analysis used δ. To facilitate mixed-mode coupling, this analysis additionally considered changes in D during damage evolution.

The next step is to update damage state whenever current tractions cause new damage. During displacement-driven numerical modeling, each step involves an increment in displacement, du. First, calculate a trial traction:

$$T^{(trial)} = k(1-D)(u+du)$$

If this traction is below the current strength (*i.e.*, $T^{(trial)} \leq S(\delta)$), the deformation is elastic — the trial traction is accepted and no changes are made to damage state variables. But, if $T^{(trial)} > S(\delta)$, the damage state evolves to keep updated traction equal to updated strength:

$$T + \nabla T \cdot (du, dD) = S(\delta) + S'(\delta)d\delta \quad \Longrightarrow \quad \nabla T \cdot (du, dD) = S'(\delta)d\delta$$

where the final form realizes that infinitesimal damage evolution always starts on the failure surface or $T = S(\delta)$. Solving the above equation for increment in δ can be cast as:

$$d\delta = \frac{k(1-D)du}{S'(\delta) + ku\mathbb{R}(\delta)} \tag{6}$$

where $\mathbb{R}(\delta)$ is newly-defined function that relates evolution in D to evolution in δ:

$$\mathbb{R}(\delta) = \frac{dD}{d\delta} = \frac{\varphi(\delta)}{k\delta^2} \quad \text{where} \quad \varphi(\delta) = S(\delta) - \delta S'(\delta) \tag{7}$$

Substituting $\mathbb{R}(\delta)$, using Eq. (4), and realizing that $u = \delta$ during damage evolution, this damage update reduces to $d\delta = du$. This result is obvious by prior definition of $\delta = \max(u)$, but a derivation based on changes in traction clarifies its connection to a strength model.

Yet another option is to define a traction failure surface depending on the current damage state. In unidirectional loading, the failure surface is a point in 1D space defined by $S(\delta)$. A failure surface analysis asserts that trial traction exceeding the current strength, *returns* to an updated failure surface by a justifiable path. In 1D analysis, the only possible path requires:

$$\frac{T(u+du)}{S(\delta+d\delta)} = \frac{u+du}{\delta+d\delta} = 1 \quad \Longrightarrow \quad d\delta = u - \delta + du \tag{8}$$

Realizing that $u = \delta$ during damage evolution, this approach likewise reduces to $d\delta = du$.

A good reason for using cohesive zones is to model crack-tip process zones. A less compelling reason for using them is as a numerical hack to mimic crack formation and propagation when explicit crack modeling is too cumbersome. By either reason, CZM is connected to material failure properties by area under the cohesive law being equal to material toughness, G_c, such that decohesion occurs when energy dissipated by the cohesive zone reaches G_c. Some mixed-mode tasks below require tracking increments in dissipated energy. In 1D analysis, that increment is $d\Omega = -d\Pi = d(W-U)$ where Π is potential energy, W is work done on the zone, and U is strain energy remaining in the zone [21]. The cumulative energy released per unit cohesive zone area up to u is:

$$\Omega = W - U = \int_0^u F(u)\,du - \frac{1}{2}\frac{S(\delta)}{\delta}u^2$$

The first term is work from area under the cohesive law up to u while the second term subtracts remaining strain energy from area under the unloading curve; *i.e.*, Ω is the shaded area in Fig. 1. The incremental energy released becomes:

$$\frac{d\Omega}{du} = F(u) - \frac{u}{\delta}S(\delta) + \frac{u^2}{2}\frac{\varphi(\delta)}{\delta^2}\frac{d\delta}{du}$$

For monotonic loading and $u < u^{(e)}$, $F(u) = ku$, $\delta = u^{(e)}$, and $\varphi(u^{(e)}) = 0$ leading correctly to no energy dissipation during initial elastic loading. For $u > u^{(e)}$, $u = \delta$ and $F(u) = S(\delta)$ during damage evolution results in

$$d\Omega = \frac{1}{2}\varphi(\delta)d\delta \tag{9}$$

indicating that $\varphi(\delta)$ is an energy dissipation rate function for variations in δ. This same result can be derived directly from strain energy by [21]

$$d\Omega = -\left(\frac{\partial U(u,D)}{\partial D}\right)_u dD = \frac{1}{2}ku^2 dD = \frac{1}{2}ku^2\mathbb{R}(\delta)d\delta = \frac{1}{2}\left(\frac{u}{\delta}\right)^2\varphi(\delta)d\delta$$

For 1D damage evolution when $u = \delta$, these two forms are identical. Increments with $u \neq \delta$ are needed in mixed-mode loading. Because $dD \geq 0$ and $dD = 0$ during elastic increments, these expressions guarantee that $d\Omega \geq 0$ and that elastic steps conserve energy. The increment in terms of δ places limits on acceptable strength models — all such models must have $\varphi(\delta) \geq 0$. For example, the strength model in Fig. 1 is not monotonically decreasing, but does satisfy $\varphi(\delta) \geq 0$ for all δ. While strength need not monotonically decrease, the stiffness must monotonically decrease as damage evolves:

$$\frac{dk_{eff}}{d\delta} = -k\frac{dD}{d\delta} = -k\mathbb{R}(\delta) = -\frac{\varphi(\delta)}{\delta^2}$$

Thus $\varphi(\delta) \geq 0$ guarantees both $dk_{eff} \leq 0$ and $d\Omega \geq 0$. No other limitations on strength models are needed.

2.2. Mixed Mode Modeling

Mixed-mode modeling begins by defining two strength models, $S_n(\delta_n)$ and $S_t(\delta_t)$, for normal and tangential directions that depend on two separate (for now) damage state variables — δ_n and δ_t (an option to have these strengths depend on both damage variables is discussed below). The normal and tangential tractions independently follow Eq (2) leading to:

$$T_n = \frac{S_n(\delta_n)}{\delta_n}u_n, \quad T_t = \frac{S_t(\delta_t)}{\delta_t}u_t, \quad U(\boldsymbol{u},\boldsymbol{\delta}) = \int_0^{\boldsymbol{u}} \boldsymbol{T}\cdot d\boldsymbol{u} = \frac{1}{2}\frac{S_n(\delta_n)}{\delta_n}u_n^2 + \frac{1}{2}\frac{S_t(\delta_t)}{\delta_t}u_t^2 \tag{10}$$

where $\boldsymbol{u} = (u_n, u_t)^T$ is zone displacement vector with normal (u_n) and tangential (u_t) components. The scalar D is replaced by a second-rank tensor defined by $\boldsymbol{u}_{damage} = \mathbf{D}\boldsymbol{u}$ analogous to methods in anisotropic damage mechanics [8, 10]. The tractions and strain energy become

$$\boldsymbol{T} = \mathbf{K}(\mathbf{I}-\mathbf{D})\boldsymbol{u} \quad \text{and} \quad U(\boldsymbol{u},\mathbf{D}) = \frac{1}{2}\mathbf{K}(\mathbf{I}-\mathbf{D})\boldsymbol{u}\cdot\boldsymbol{u}$$

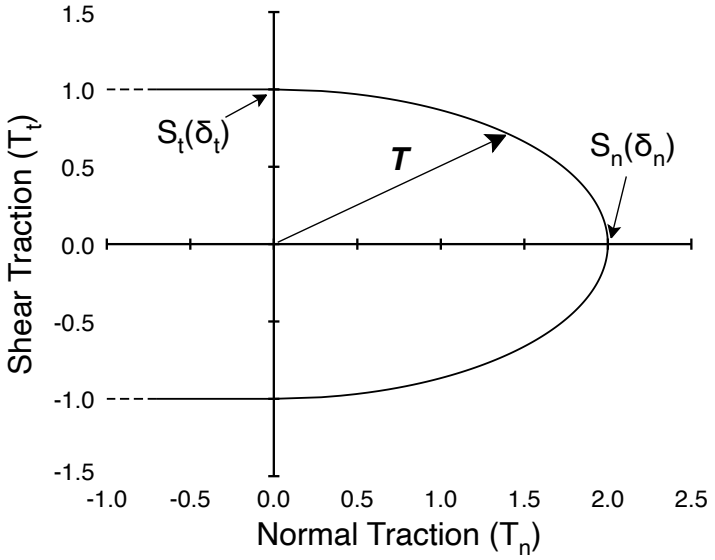

Figure 2: The traction-failure surface used in modeling. The right half is for zones in tension and is an elliptical function of normal and tangential tractions. The left half is for compression or when zone surfaces are in contact. In compression, failure occurs only by tangential traction.

where $\mathbf{K}$ is initial stiffness tensor. Comparing to Eq. (10) leads to $\mathbf{K} = \text{diag}(k_n, k_t)$ with initial normal and tangential stiffnesses and $\mathbf{D} = \text{diag}(D_n, D_t)$ with two separate (for now) damage parameters each defined by Eq. (4). The energy dissipation increment per unit area becomes:

$$\begin{aligned} d\Omega &= -\left(\frac{\partial U(\boldsymbol{u}, \mathbf{D})}{\partial \mathbf{D}}\right)_{\boldsymbol{u}} d\mathbf{D} = \frac{1}{2} k_n u_n^2 dD_n + \frac{1}{2} k_t u_t^2 dD_t \\ &= d\Omega_I + d\Omega_{II} = \frac{1}{2}\left(\frac{u_n}{\delta_n}\right)^2 \varphi_n(\delta_n) d\delta_n + \frac{1}{2}\left(\frac{u_t}{\delta_t}\right)^2 \varphi_t(\delta_t) d\delta_t \end{aligned} \tag{11}$$

The released energy partitions into sum of mode I and mode II energy dissipation increments. Because mixed-mode damage evolution, in general, occurs when $u_n < \delta_n$ and $u_t < \delta_t$, energy increments must retain the u/δ terms not needed in 1D methods (*i.e.*, Eq. (9)). Furthermore, δ_n and δ_t are no longer given by $\max(u_n)$ or $\max(u_t)$; new damage evolution methods are needed.

The next step is to derive a mixed-mode strength model to predict failure under combined normal and tangential traction. This modeling assumed a failure surface given by:

$$\left(\frac{\langle T_n \rangle_+}{S_n(\delta_n)}\right)^2 + \left(\frac{T_t}{S_t(\delta_t)}\right)^2 = 1 \tag{12}$$

where $\langle T_n \rangle_+$ is zero in compression but T_n in tension. This surface, which is plotted in Fig. 2, predicts failure when traction vector, $\boldsymbol{T}$, reaches the surface. The tensile half plane is a half ellipse. The compression half plane predicts only tangential failure.

A mixed-mode strength model is derived by finding the traction magnitude needed to reach the surface as a function of δ_n, δ_t, and the current mode-mixity. In other words, while 1D

strength models are 2D plots of $S(\delta)$ as a function of δ, mixed-mode strength models are 4D plots for strength as a function of δ_n, δ_t, and θ where θ is mode-mixity defined here by

$$\tan\theta = \frac{u_n}{u_t} \quad \Longrightarrow \quad u_n = \|\boldsymbol{u}\|\sin\theta \text{ and } u_t = \|\boldsymbol{u}\|\cos\theta \tag{13}$$

where $\theta = \pi/2$ for pure mode I and $\theta = 0$ or π for pure mode II. In the tensile half plane ($0 < \theta < \pi$), the traction magnitude is:

$$\|\boldsymbol{T}\| = \|\boldsymbol{u}\|\sqrt{\frac{S_n(\delta_n)^2}{\delta_n^2}\sin^2\theta + \frac{S_t(\delta_t)^2}{\delta_t^2}\cos^2\theta}$$

This traction reaches the elliptical failure surface when $\|\boldsymbol{u}\| \to \delta_d$ such that

$$\left(\frac{T_n}{S_n(\delta_n)}\right)^2 + \left(\frac{T_t}{S_t(\delta_t)}\right)^2 = \delta_d^2\left(\frac{\sin^2\theta}{\delta_n^2} + \frac{\cos^2\theta}{\delta_t^2}\right) = 1 \implies \delta_d = \frac{1}{\sqrt{\frac{\sin^2\theta}{\delta_n^2} + \frac{\cos^2\theta}{\delta_t^2}}}$$

The mixed-mode strength model is then given by traction magnitude when $\|\boldsymbol{u}\| = \delta_d$:

$$S(\delta_n, \delta_t, \theta) = \sqrt{\frac{\frac{S_n(\delta_n)^2}{\delta_n^2}\sin^2\theta + \frac{S_t(\delta_t)^2}{\delta_t^2}\cos^2\theta}{\frac{\sin^2\theta}{\delta_n^2} + \frac{\cos^2\theta}{\delta_t^2}}}$$

The distinction between strength model and cohesive laws, which is semantics for 1D, is a key concept in mixed-mode CZM. 1D modeling seemingly evaluates strength and traction from the same function, which has caused understandable confusion about its physical interpretation. In contrast, mixed-mode modeling evaluates tractions from independent normal and tangential strength models, while the mixed-mode strength model, $S(\delta_n, \delta_t, \theta)$, couples them to define a traction failure surface. Numerous CZM results can be generated by selecting various unidirectional strength models. Entirely new classes of CZM could be developed by postulating new zone-failure mechanics; *i.e.*, by changing the failure criterion in Eq. (12) from an elliptical surface to some other shape.

The method to update mixed-mode damage variables in the tensile half plane can reprise the three methods used in 1D. The first method equates traction increment to strength change, now using strength gradient:

$$\nabla\|\boldsymbol{T}\| \cdot (u_n, u_t, D_n, D_t) = \nabla S(\delta_n, \delta_t, \theta) \cdot (\delta_n, \delta_t, \theta)$$

The second method notes that δ_d remains equal to $\|\boldsymbol{u}\|$ during damage evolution, which leads to update equation of $d\delta_d = d\|\boldsymbol{u}\|$. The third method requires a trial traction exceeding the failure surface to return to an updated failure surface by solving:

$$\left(\frac{T_n(u_n + du_n)}{S_n(\delta_n + d\delta_n)}\right)^2 + \left(\frac{T_t(u_t + du_t)}{S_t(\delta_t + d\delta_t)}\right)^2 = \left(\frac{u_n + du_n}{\delta_n + d\delta_n}\right)^2 + \left(\frac{u_t + du_t}{\delta_t + d\delta_t}\right)^2 = 1 \tag{14}$$

All three methods were used and satisfyingly, all three led to the same update equation. The simplest method is the return method. Expanding Eq. (14) in a Taylor series and keeping only first order terms in the increments quickly leads to:

$$\frac{u_n^2}{\delta_n^3} d\delta_n + \frac{u_t^2}{\delta_t^3} d\delta_t = \frac{u_n}{\delta_n^2} du_n + \frac{u_t}{\delta_t^2} du_t \tag{15}$$

For 1D loading, this equation correctly reverts to $d\delta_n = du_n$ or $d\delta_t = du_t$.

Equation (15) is a new concept in CZM literature, but it only provides a single equation to update two damage variables. To complete the update we need a second equation, which is derived by requiring the desirable property that normal and tangential tractions simultaneously reach zero at decohesion. This goal is achieved by asserting that $D_n = D_t = D$. Using $\mathbb{R}_n(\delta_n) = dD_n/d\delta_n$ and $\mathbb{R}_t(\delta_t) = dD_t/d\delta_t$, the final updates become:

$$dD = \frac{\frac{u_n}{\delta_n^2} du_n + \frac{u_t}{\delta_t^2} du_t}{\frac{1}{\mathbb{R}_n(\delta_n)} \frac{u_n^2}{\delta_n^3} + \frac{1}{\mathbb{R}_t(\delta_t)} \frac{u_t^2}{\delta_t^3}}, \qquad d\delta_n = \frac{dD}{\mathbb{R}_n(\delta_n)}, \qquad d\delta_t = \frac{dD}{\mathbb{R}_t(\delta_t)}, \tag{16}$$

Once these increments are found, incremental released energies ($d\Omega_I$ and $d\Omega_{II}$) are found by Eq. (11). As in 1D, a mixed-mode return analysis starts out independent of the strength models (see Eqs. (14) and (15)). 1D methods require no additional coupling and thus 1D updates are entirely independent of its strength model. In contrast, coupling the mixed-mode damage variables leads to final mixed-mode updates that depend on the strength models through $\mathbb{R}_n(\delta_n)$ and $\mathbb{R}_t(\delta_t)$ in Eq. (16).

Besides simply asserting $D_n = D_t$, three alternatives for returning to the traction-failure surface were considered: 1. return normal to the surface; 2. return by a path that minimizes dissipated energy; 3. return parallel to the current traction vector. Method 1 is imposing plasticity methods on elastic/damage response. It fails to satisfy the requirement that normal and tangential tractions simultaneously decay to zero. In other words, despite similarities, plasticity methods may not apply when using damage mechanics methods. Method 2 fails because the minimum energy path is always on the extrema (*i.e.*, damage update would be modeled as either all $d\delta_n$ or all $d\delta_t$). In some cases, that path allows pure mode I loading to induce only mode II damage. Finally, method 3 worked and led to same conclusion that $D_n = D_t$. In other words, the assertion $D_n = D_t$ in mixed-mode damage is equivalent to returning to the failure surface parallel to the current traction vector.

Different methods are needed for the compression half plane. Because the failure surface depends only on tangential traction, damage evolution reduces to a 1D analysis or $d\delta_t = du_t$. The modeling, however, needs to maintain constant D, which implies additional updates of

$$dD = \mathbb{R}_t(\delta_t) d\delta_t \quad \text{and} \quad d\delta_n = \frac{\mathbb{R}_t(\delta_t) d\delta_t}{\mathbb{R}_n(\delta_n)} \tag{17}$$

Despite damage evolving in both normal and tangential directions, this update releases only mode II energy. The mode I component ($d\Omega_I$ in Eq. (11)) is zero because $u_n = 0$ when cohesive zone surfaces are in contact.

Finally, extending the above analysis is 2D to 3D is straightforward. In 3D, the transverse deflection vector would resolve into $\boldsymbol{u}_t = (u_{t1}, u_{t2})$. Including two shear terms in Eq. (14) extends Eq. (15) to 3D evolution of

$$\frac{u_n^2}{\delta_n^3} d\delta_n + \frac{u_{t1}^2}{\delta_{t1}^3} d\delta_{t1} + \frac{u_{t2}^2}{\delta_{t2}^3} d\delta_{t2} = \frac{u_n}{\delta_n^2} du_n + \frac{u_{t1}}{\delta_{t1}^2} du_{t1} + \frac{u_{t2}}{\delta_{t2}^2} du_{t2} \tag{18}$$

If the sliding properties of the interface are isotropic (*i.e.*, $\delta_{t1} = \delta_{t2} = \delta_t$ and $S_{t1}(\delta_{t1}) = S_{t2}(\delta_{t2}) = S_t(\delta_t)$), this 3D update reduces to the 2D update where u_t is replaced by $\|\boldsymbol{u}_t\|$; *i.e.*, it suffices to resolve $\boldsymbol{u}$ into displacements normal and tangential to the interface [22]. Extension to 3D modeling of anisotropic interfaces would need a second tangential strength model along with terms for an extra damage parameter in Eq. (16). Another 3D issue is separation of shear failure into mode II and mode III. That separation would require further resolution of $\boldsymbol{u}$ into tangential displacements parallel and perpendicular to the crack front. Because cohesive zones are local descriptions of interfacial deformation not connected to a crack front, however, that calculation is not possible in this or any prior CZM method. The standard approach is to lump shear failure into a single process, which is labeled here as mode II but actually would mode II and mode III in 3D. Although individual cohesive zones cannot identify mode III, numerical modeling of global mode II and mode III failures with a collection of cohesive zones could provided insights into difference between those failure processes.

2.3. Special Cases

2.3.1. No Initial Elastic Deformation

The Taylor expansion used for Eq. (16) assumed $\delta_n \gg d\delta_n$ and $\delta_t \gg d\delta_t$, which is typically true for any strength model with an initial elastic region (*i.e.*, $\delta \geq u^{(e)} > 0$). But some CZM has nonlinear response from the beginning (*e.g.*, cubic or exponential laws [17, 18]) or might have very high initial stiffness causing very small $u^{(e)}$. A general approach for such strength models is to rewrite Eq. (14) in terms of D:

$$\left(\frac{u_n + du_n}{\delta_n(D+dD) + \frac{dD}{\mathbb{R}_n\left(\delta_n(D+dD)\right)}} \right)^2 + \left(\frac{u_t + du_t}{\delta_t(D+dD) + \frac{dD}{\mathbb{R}_t\left(\delta_t(D+dD)\right)}} \right)^2 = 1 \tag{19}$$

and solve numerically for dD using Newton's method with bracketing of $0 < dD < 1 - D$.

2.3.2. Tangential Strength is Scaled Copy of Normal Strength

Imagine the special case where the tangential strength model is derived from the normal strength model by scaling the x and y axes or

$$S_t(\delta_t) = \frac{\sigma_{tc}}{\sigma_{nc}} S_n\left(\frac{\delta_t}{\chi}\right), \qquad G_{IIc} = \frac{\sigma_{tc}\chi}{\sigma_{nc}} G_{Ic}, \quad \text{and} \quad k_t = \frac{\sigma_{tc}}{\sigma_{nc}\chi} k_n \tag{20}$$

where σ_{tc} and σ_{nc} are maxima tangential and normal strengths and χ is a constant. By invoking $D_n = D_t = D$ during damage evolution using Eq. (4), this special case implies $\chi = \delta_t/\delta_n$.

In other words, δ_t evolves proportionally to δ_n. From their decohesion values, their constant ratio must be $\chi = u_t^{(c)}/u_n^{(c)} = r_c$. If $u_n^{(e)} > 0$, the ratio is also $\chi = u_t^{(e)}/u_n^{(e)} = r_e$, which implies the ratios of elastic to failure displacements are the same: $r_e = r_c \implies u_t^{(e)}/u_t^{(c)} = u_n^{(e)}/u_n^{(c)}$. With such proportional damage variables, the return analysis in Eq. (14) can be solved directly using a single damage variable:

$$\frac{\delta_n + d\delta_n}{u_n^{(c)}} = \sqrt{\left(\frac{u_n + du_n}{u_n^{(c)}}\right)^2 + \left(\frac{u_t + du_t}{u_t^{(c)}}\right)^2}$$

We can define an *effective* displacement by Eq. (1) and model using a single damage state variable that evolves by $\delta_n = u_n^{(c)} \max(u_{eff})$. In other words, this special case reduces mixed-mode analysis to be equivalent to a 1D, effective displacement analysis. As a corollary, however, if normal and tangential models are not scaled copies, effective displacement methods [14–16] are all invalid and must be replaced with the updates in Eq. (16).

2.3.3. Strength Variations

Both strength CZM and all prior CZM assume cohesive laws depend only on the current damage state. This re-evaluation in terms of strength models now raises the question — what happens if strength depends on external variables such as temperature, pressure, moisture content, strain rate, *etc.*? Generalizing strength models proceeds by changing them to $S(\delta, \boldsymbol{\alpha})$ where $\boldsymbol{\alpha}$ is a vector of all quantities affecting strength. The incremental D–δ relation, now including dependence on $\boldsymbol{\alpha}$, can be cast as:

$$dD = \left(\frac{\partial D}{\partial \delta}\right)_{\boldsymbol{\alpha}} d\delta + \left(\frac{\partial D}{\partial \boldsymbol{\alpha}}\right)_{\delta} \cdot d\boldsymbol{\alpha} = \mathbb{R}(\delta, \boldsymbol{\alpha})\left(d\delta - d\delta^{(e)}\right)$$

where $d\delta^{(e)}$ is change in δ that occurs during elastic deformation when $dD = 0$. It evaluates to:

$$d\delta^{(e)} = \frac{\delta}{\varphi(\delta, \boldsymbol{\alpha})} \sum_i \left(\frac{\partial S(\delta, \boldsymbol{\alpha})}{\partial \alpha_i}\right)_{\delta, \alpha_{j \neq i}} d\alpha_i$$

Expanding strength as $S(\delta + d\delta, \boldsymbol{\alpha} + d\boldsymbol{\alpha}) = S'(\delta, \boldsymbol{\alpha}) d\delta + \varphi(\delta, \boldsymbol{\alpha}) d\delta^{(e)}/\delta$ and revising derivation of Eq. (6) again leads to a 1D update of $d\delta = du$, but with one important difference. The damage variable δ must change by $d\delta^{(e)}$ during elastic unloading and reloading. Because it may increase or decrease in elastic steps, δ will no longer equal $\max(u)$ — it will equal the u required to induce damage for current $\boldsymbol{\alpha}$. This need to update δ variables even during elastic deformation is new concept in CZM. Because mixed-mode updates depend on strength models (see Eq. (16)), its generalizations to $\boldsymbol{\alpha}$ variables requires more work. These generalizations should be the subject of future publications.

3. Results and Discussion

3.1. Cohesive Zone Implementation

Strength CZM methods were implemented in material point method (MPM) code by extending methods in Ref. [23] using steps outlined in Appendix A. Implementation in finite

element analysis (FEA) could use the tangent stiffness matrix derived in Appendix B. This MPM implementation allowed strength models based on sawtooth, trilinear, or cubic cohesive laws. We note, however, that strength CZM was derived without reference to specific cohesive laws. It was instead derived by considering physical mechanisms in the process zone. The mechanism assumed here was an elastic/damage zone. Other strength CZM methods might consider plasticity or damage combined with plasticity. The cohesive laws are only needed for final implementation and coding only needs methods to evaluate $S(\delta)$, $S'(\delta)$, and $\delta(D)$ for normal and tangential strength models (other functions, $\varphi(\delta)$, $\mathbb{R}(\delta)$, and $D(\delta)$, can be derived from these basic functions). The strength models used here (see Appendix C for their basic functions) were chosen because $\delta(D)$ can be expressed analytically. Models that require numerical inversion of $D(\delta)$ are less efficient.

3.2. Comparison to Prior Methods

For comparison purposes, the decoupled approach [13] and a coupled approach based on *effective* displacements [16] were both implemented. The decoupled approach used 1D damage-evolution methods, but to predict failure, it needs a decohesion criterion. This implementation assumed failure in the decoupled approach occurs when

$$\left(\frac{G_I}{G_{Ic}}\right)^p + \left(\frac{G_{II}}{G_{IIc}}\right)^p = 1 \tag{21}$$

where p is a cohesive zone property.

The implemented *effective* displacement model was from Högberg [16]. This model defines an effective displacement by $\lambda = u_{\mathit{eff}}$ in Eq. (1). Zone tractions after initiation are defined in terms of a damage parameter, ω, by:

$$\boldsymbol{T} = \frac{1-\omega}{\lambda_p(\theta')}\left(\frac{\sigma_{nc}u_n}{u_n^{(c)}}, \frac{\sigma_{tc}u_t}{u_t^{(c)}}\right), \quad \omega = 1 - \frac{H(\lambda_\omega)\lambda_p(\theta')}{\lambda_\omega}, \quad \text{and} \quad H(\lambda) = \frac{1-\lambda}{1-\lambda_p(\theta')} \tag{22}$$

Here $\lambda_\omega = \max(\lambda)$ is a damage state variable that evolves from $\lambda_p(\theta')$ at initiation to 1 at decohesion and θ' changes mode-mixity angle in Eq. (13) to $\tan\theta' = (u_t^{(c)}/u_n^{(c)})\tan\theta$ [16]. $H(\lambda)$ is a normalized strength model that decays from 1 when $\lambda = \lambda_p(\theta')$ to zero when $\lambda = 1$. Högberg assumed the linear model in Eq. (22), but the approach is easily extended to any $H(\lambda) = S(\lambda u^{(c)})/\sigma_c$. Physically, $\lambda_p(\theta')$ is the λ to initiate damage assuming an elliptical failure criterion [16]:

$$\frac{1}{\lambda_p(\theta')} = \sqrt{\left(\frac{u_n^{(c)}\sin\theta'}{u_n^{(e)}}\right)^2 + \left(\frac{u_t^{(c)}\cos\theta'}{u_t^{(e)}}\right)^2} \tag{23}$$

A problem with the Högberg model is that damage parameter ω depends on θ'. As a consequence, if mode mixity changes during elastic unloading and reloading, ω will change resulting in elastic deformations that do not conserve energy. Even if mode mixity remains constant (or if one chooses to hold $\lambda_p(\theta')$ constant at its initiation value), this model unrealistically causes the ratio of normal to tangential stiffness to jump from k_n/k_t before initiation to

$u_n^{(e)}u_t^{(c)}k_n/(u_t^{(e)}u_n^{(c)}k_t)$ after initiation. Both these problems disappear whenever $\lambda_p(\theta')$ is independent of θ', which by Eq. (23) implies the Högberg model is limited to $u_n^{(e)}/u_n^{(c)} = u_t^{(e)}/u_t^{(c)}$ (*i.e.*, $r_e = r_c$). With this limitation, the Högberg model reduces to the special case of strength CZM given in Section 2.3.2 with $\lambda = \delta_n/u_n^{(c)} = \delta_t/u_t^{(c)}$. Without this limitation, as claimed acceptable in Ref. [16], the model is always invalid for mixed-mode loading.

Energy calculations described below require tracking incremental dissipations or $d\Omega_I$ and $d\Omega_{II}$. Reference [16] only provides *total* energy released; increments are found by transforming Eq. (11) to the normalized Högberg λ variable:

$$d\Omega = \frac{1}{2}\left(\sigma_{nc}u_n^{(c)}\sin^2\theta' + \sigma_{tc}u_t^{(c)}\cos^2\theta'\right)\left(H(\lambda_\omega) - \lambda_\omega H'(\lambda_\omega)\right)d\lambda_\omega$$

Using linear $H(\lambda)$ yields:

$$d\Omega_I = \frac{G_{Ic}\sin^2\theta'}{1-\lambda_p(\theta')}d\lambda_\omega \qquad \text{and} \qquad d\Omega_{II} = \frac{G_{IIc}\cos^2\theta'}{1-\lambda_p(\theta')}d\lambda_\omega \tag{24}$$

In this model, these increments are only valid when $\lambda_p(\theta')$ is constant. When valid, they integrate as λ_ω evolves from $\lambda_p(\theta')$ to 1 to the Högberg total energies of $\Omega_I = G_{Ic}\sin^2\theta'$ and $\Omega_{II} = G_{IIc}\cos^2\theta'$ [16]. For comparison purposes, the Högberg model was implemented to allow independent sawtooth laws, even though this allowance causes invalid modeling.

Other effective displacement methods simply use $u_{eff} = \|\boldsymbol{u}\|$ [15], which is equivalent to requiring strength models scaled by Eq. (20) and choosing $r_c = r_e = 1$. This approach is a special case of Högberg when $u_t^{(c)} = u_n^{(c)}$ and $u_t^{(e)} = u_n^{(e)}$, and it is only valid when these conditions hold. It also corresponds to cohesive elements in Abaqus based on $\delta_m = \|\boldsymbol{u}\|$ [24]; unfortunately, Abaqus allows users to choose properties that violate these validity conditions.

Methods that couple through cohesive laws [11, 17, 18, 25, 26] could be implemented in this analysis by reinterpreting those tractions as strength models. Such an approach begins by changing $S_n(\delta_n)$ to $S_n(\delta_n, \delta_t)$ and $S_t(\delta_t)$ to $S_t(\delta_n, \delta_t)$. Much of this new analysis is unaffected by this extra coupling. For example the update in Eq. (15) is valid because it is independent of the strength models. But coupling in strength models complicates other steps. For example, energy dissipation in Eq. (11) changes to:

$$d\Omega = \frac{1}{2}\left(k_n u_n^2, k_t u_t^2\right)\cdot(\mathbf{R}\,d\boldsymbol{\delta}) \quad \text{with} \quad \mathbf{R}_{ij} = \frac{\partial D_i}{\partial \delta_j} \text{ where } i,j = n\ (1) \text{ or } t\ (2) \tag{25}$$

The damage evolution in Eq. (16) changes to:

$$dD = \frac{\frac{u_n}{\delta_n^2}du_n + \frac{u_t}{\delta_t^2}du_t}{\frac{1}{\mathbf{R}_{nn}^{-1}+\mathbf{R}_{nt}^{-1}}\frac{u_n^2}{\delta_n^3} + \frac{1}{\mathbf{R}_{tn}^{-1}+\mathbf{R}_{tt}^{-1}}\frac{u_t^2}{\delta_t^3}}$$

While these generalization to coupled strength models could be implemented, the wisdom of that effort is difficult to justify. First, CZM results depend on peak stress and toughness, but

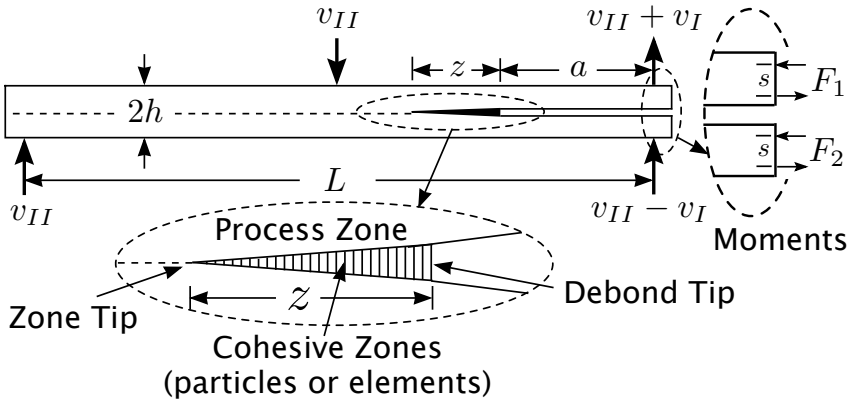

Figure 3: Cracked Beam specimen loaded in mixed-mode Bending (CBB) by varying velocities v_I and v_{II}. The specimen has an initial crack of length a with remaining specimen length consisting of a line of inserted cohesive zones (particles or elements). When loaded, the crack tip develops a process zone of length z for cohesive zones beyond their elastic limit. The bottom inset magnifies the process zone and defines the "Zone Tip" and "Debond Tip" locations. The right inset shows boundary conditions used for pure moment loading.

are relatively insensitive to strength model shape [1]. It is likely a fool's errand to think choosing between strength models with the same peak stress and toughness is a crucial task in CZM. Second, coupling in strength models introduces coupling between mode I and mode II energy dissipation due to off-diagonal terms in Eq. (25). In other words, energy dissipation with such strength models differs from the usual mode decoupling in fracture mechanics [21]. Third, coupled tractions in prior models were chosen by comparison to reversible, atomic binding energies [18]. This concept of seeking a "potential" that can be differentiated to find tractions is inconsistent with re-evaluating CZM in terms of strength models instead of "traction laws." While elastic tractions can be found from potential energies, strengths are failure properties that may not be connected to a potential.

3.3. Cohesive Zone Crack Propagation and Mode Mixity

In linear elastic fracture mechanics (LEFM), crack-tip displacements can be partitioned into mode I (opening) and mode II (sliding) displacements with magnitudes characterized by stress intensity factors, K_I and K_{II} [21]. Mode mixity characterization is clear and K_I and K_{II} are independent of material properties. In CZM, the inserted cohesive zones are extending LEFM to include a process zone. Mode mixity characterization needs extending as well and the results will depend on zone properties. A crack-tip process zone replaces the single crack tip in LEFM with two tips — one at the leading edge (zone tip) and one at the trailing edge (debond tip) of the zone (see Fig. 3) [19]. Crack growth involving process zones has three possible phases:

1. *Elastic Loading* — as long as no cohesive zone exceeds $u_n^{(e)}$ or $u_t^{(e)}$, the deformation is elastic with no energy dissipation.

2. *Process Zone Development* — once elastic limit is exceeded, cohesive zones start to dissipate energy. Defining process zone length as the extent of cohesive zones with $0 < D < 1$, this phase

corresponds to zone tip propagation alone. The debond tip remains fixed and the process zone length increases.

3. *Decohesion* — once $D \to 1$ at the debond tip, the decohesion phase starts where debond-tip propagation occurs along with zone-tip propagation. If process zone length remains constant, the crack growth can be characterized as self-similar crack propagation (*i.e.*, debond tip, zone tip and all damage translate together). The natural process zone length, however, depends on mode mixity. As a consequence, if mode mixity changes during decohesion, the process zone length will change and the crack growth will be non-self similar.

Because some (or all) crack growth with process zones may be non-self similar, care is needed when defining energy release rates and calculating mode mixity. For CZM with elastic/damage process zones, all energy dissipation occurs in the cohesive zones. Imagine a line ahead of a crack tip that is modeled by discretization into N cohesive zones. Total mode I and II dissipated energies become:

$$\Gamma_I(t) = \sum_{i=1}^{N} \Omega_I^{(i)}(t) A^{(i)} \quad \text{and} \quad \Gamma_{II}(t) = \sum_{i=1}^{N} \Omega_{II}^{(i)}(t) A^{(i)}$$

where $\Omega_I^{(i)}(t)$ and $\Omega_{II}^{(i)}(t)$ are cumulative energies dissipated per unit area by cohesive zone i with area $A^{(i)}$. To enable these calculations, CZM must accumulate increments in dissipated energy using Eq. (11). Fracture mechanics energy release rates (*i.e.*, energy released per unit crack growth), are then found from slopes of $\Gamma_I(t)$ and $\Gamma_{II}(t)$ when cross plotted as functions of crack area. In 2D, $A(t) = ba(t)$ where b is width and $a(t)$ is crack length giving:

$$G_I = \frac{1}{b}\frac{d\Gamma_I(t)}{da(t)} \quad \text{and} \quad G_{II} = \frac{1}{b}\frac{d\Gamma_{II}(t)}{da(t)} \tag{26}$$

These energy release rates model a material's R curve or fracture toughness as a function of crack growth. Such R curves depend on whether crack length $a(t)$ is determined by debond-tip or zone-tip propagation. These two options will be called the debond-tip R curve and the zone-tip R curve.

When using CZM to interpret experiments, one must begin by assessing whether reported "crack lengths" are based on debond tip or zone tip propagation. The answer depends on experimental methods used to locate the crack tip. For adhesive joints failing with microvoids and microcracks, experiments are more likely observing the debond tip. In contrast, for composite delamination [1] or wood fracture [27–30] failing with fiber bridging, experiments are more likely (or deliberately [27]) observing the zone tip. When modeling experimental results for zone-tip propagation, the numerical methods need to locate their zone tip as well. For strength models with an initial elastic regime, the zone tip is the leading edge among all cohesive zones with $D > 0$. In contrast, strength models with no initial elastic region start with zero strength meaning all zones will develop damage ($D > 0$) after any deformation. Such models could resort to finding zone tip from zones with $\Omega_I + \Omega_{II} > \Omega_{min}$, where Ω_{min} is a suitably small, non-zero value.

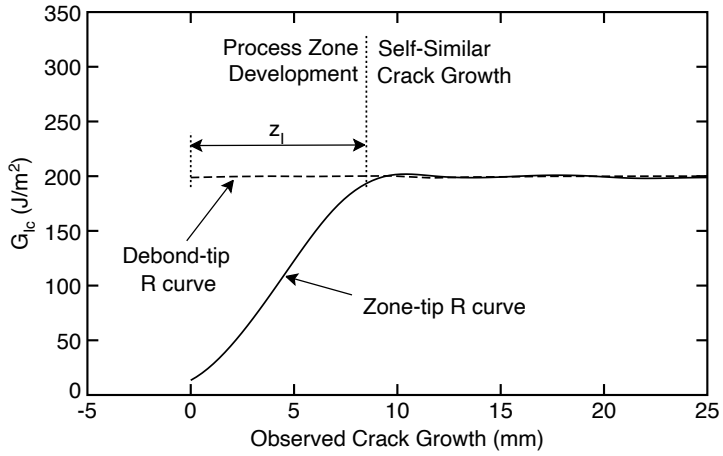

Figure 4: Mode I R curves from CZM simulations determined by differentiation of $\Omega(t)$ with respect to zone-tip propagation (solid curve) or debond-tip propagation (dashed curve). The steady-state process zone length was $z_I = 8.5$ mm and that length remained constant during steady-state crack propagation.

To illustrate consequences of two crack tips, simulations were run for a Cracked Beam specimen loaded in Bending (CBB) as shown in Fig. 3 with $L = 200$ mm and $h = 10$ mm for isotropic, linear elastic arms with modulus $E = 3$ GPa, Poisson's ratio $\nu = 0.33$, and density $\rho = 1$ g/cm^3. An explicit MPM crack [31, 32] was placed along the beam's midplane. A distance $a = 50$ mm was an initial crack while remaining specimen length was initialized with cohesive zones between crack surfaces. The mode I and II strength models were based on sawtooth cohesive laws with $G_{Ic} = 200$ J/m^2 and $G_{IIc} = 500$ J/m^2. The relative normal and tangential strength models were fixed to follow $r_e = 1$ and $r_c = 0.2$ resulting in relative strengths $\sigma_{tc} = \sigma_{nc}/2$. Simulations in this section used a displacement-driven, mixed-mode-bending jig [3] loaded by constant mode I and II velocities (v_I and v_{II}) — $v_I \neq 0$ with v_{II} omitted is a mode I double cantilever beam (DCB); $v_{II} \neq 0$ with $v_I = 0$ is a mode II end-notched-flexure (ENF); other conditions combine the two tests for mixed-mode loading. The velocities were adjusted to minimize inertial effects, which was achieved when the full loading time was more than 25 times the initial cantilever arm's transverse vibration time ($t_{vib} = (2\pi a^2/1.8751^2)\sqrt{12\rho/(Eh^2)}$ [33]). All 2D plane-strain MPM simulations used a regular background grid with 1×1 mm^2 cells (unless stated otherwise) and four particles per cell.

Figure 4 plots R curves for mode I DCB loading ($v_I \neq 0$, v_{II} omitted, and $\sigma_{nc} = 2$ MPa) calculated two ways. A zone-tip R curve increased from zero to a plateau value. The plateau value, equal to G_{Ic}, corresponded to self-similar crack growth because the process zone length remained constant after the onset of decohesion. The amount of crack growth required to reach the plateau was equal to the steady-state process zone length of $z_I = 8.5$ mm. In contrast, a debond-tip R curve was flat because all results were after onset of decohesion meaning all were self-similar crack propagation. In brief, if the process zone is viewed as in the wake of a crack tip, the R curve rises during process zone development and flattens in the self-similar phase. But, if the process zone is interior to a material, it represents an explanation for toughness but results in a flat R curve.

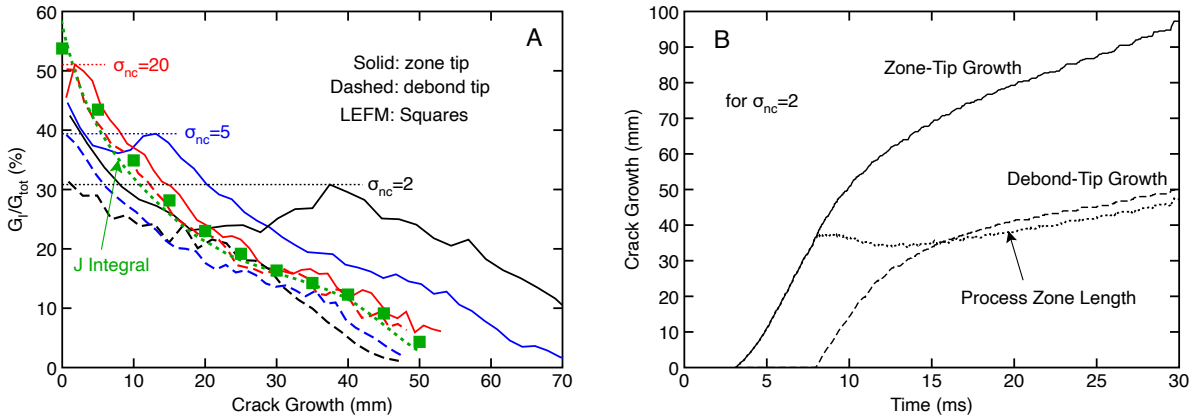

Figure 5: A. Mode mixity (% G_I) for CBB specimen loaded with $\nu_I = \nu_{II}$ for three σ_{nc} values as functions of zone-tip (solid curves) or debond-tip (dashed curves) growth. LEFM (square symbols) is mode mixity by FEA crack closure. The "J integral" (dotted curve) is mode mixity by J integral (J results were independent of σ_{nc}). B. Zone-tip and debond-tip crack growth curves for $\sigma_{nc} = 2$ MPa. Process zone length is difference between these curves.

To assess mode mixity characterization, the CBB specimen was loaded with $\nu_I = \nu_{II}$ and σ_{nc} was varied from 2 to 20 MPa. Figure 5A plots fraction G_I as a function of crack growth by the zone tip (solid curves) or the debond tip (dashed curves). CZM can become unstable for high strengths if process zone length becomes small compared to grid cells [34]. Such instabilities were resolved here by using 0.5×0.5 mm^2 cells for $\sigma_{nc} \leq 5$ MPa but using smaller 0.25×0.25 mm^2 cells for $\sigma_{nc} = 20$ MPa. Zone-tip mode mixities (solid curves) decreased and then peaked at $\Delta a = 37$, 12, and 2 mm for $\sigma_{nc} = 2$, 5, and 20 MPa, respectively, corresponding to their process zone lengths at decohesion onset. Debond-tip mode mixities (dashed curves) started at values equal to zone-tip peak values. Thereafter, zone-tip and debond-tip curves both decreased with roughly constant shifts between them. Note that consistency of these curves, despite being calculated using different cell sizes, indicates that strength CZM is insensitive to mesh size provided the cells are not too large for stable calculations. The stability limit for these calculations was found by trial and error and it agreed with Carpinteri [34] that the cell size should scale with G_c/σ_c. Calculations that violated stability limits were obviously poor and propagated with low energy. Calculations with various, sufficiently-small cell sizes were consistent.

To understand crack-tip effects, Fig. 5B plots zone-tip and debond-tip growth as a function of time for $\sigma_{nc} = 2$ MPa; the difference between them is the plotted process zone length. Up to zone-tip $\Delta a = 37$ mm at 8 ms, the zone-tip propagated, the debond-tip remained fixed, and process zone length increased. This region corresponds to zone-tip curves up to their peaks. After 8 ms, both tips propagated corresponding to post-peak zone-tip curves and entirety of the debond-tip curves. The shift between zone-tip and debond-tip mode-mixity curves matched the process zone length. Because fraction mode I decreased and a decrease in mode I caused an increase in process zone for the chosen relative strength models, both process zone length and shift between the curves increased with crack growth.

Conway *et al.* [19] advocate a similar need to use CZM to partition energy into mode I and mode II components as the partitioning depends on the cohesive zone length. Their simulations were limited to constant-mode-mixity with steady-state propagation and were based on *effective* displacement methods. They looked only at self-similar-crack propagation where cohesive zone length is constant and J-integral methods are acceptable. The use of strength CZM extends such modeling to allow non-scaled strength models and to partition mode I and mode II during non-self-similar crack propagation (even when J-integral methods do not apply). The results in Fig. 5B suggest that crack growth is never self-similar; *i.e.*, cohesive zone length is constantly changing, thereby emphasizing the need to have these new, more-general strength CZM methods.

Another question is what causes the zone-tip mode mixity to go through a minimum and then peak at the onset of decohesion? To answer, we ran a simulation for $\sigma_{nc} = 2$ MPa and $r_e = 1$, but changed to $r_c = 1$, which changed σ_{tc} from 1 MPa to 5 MPa. This higher shear strength caused the process zone length at onset of decohesion to decrease to 10.5 mm and it eliminated the peak in the mode mixity (the fraction G_I decreased monotonically with the debond-tip result again starting at same value as the zone-tip result at the onset of decohesion; results not plotted). This simulation with $r_e = r_c$ is an example of the only valid simulation possible when using *effective* displacement methods. The observation that fraction G_I changes when you change relative normal and tangential laws emphasizes the need to have strength CZM that remains valid when $r_e \neq r_c$.

For comparison, the fraction G_I by LEFM with elastic arms calculated by FEA using crack closure methods [35] is plotted in Fig. 5A (square symbols). The CZM mode mixity for $\sigma_{nc} = 2$ and 5 MPa differed significantly from LEFM but CZM approached LEFM as σ_{nc} increased to 20 MPa. These results match prior observations that CZM approaches LEFM as cohesive stress increases [1]. The reason is that high σ_{nc} leads to a small process zone. For negligible process zones, a method that accounts for them (CZM) should approach one that ignores them (LEFM).

A practical consequence of differences between CZM and LEFM is that it complicates interpretation of mixed-mode fracture experiments on materials with non-negligible process zones. Typical mixed-mode experiments start with a jig to apply mixed mode boundary conditions and then derive *a priori*, material-independent equations to partition total energy release rate, G_{tot}, into G_I and G_{II} [3, 36, 37]. The partitioning is typically done using LEFM and beam theory (for bending specimens) or FEA (for general specimens). Strength CZM results, however, show that mode mixity depends on material properties (*i.e.*, strength models) and on whether experiments observe zone tip or debond tip crack growth. In other words, one cannot rely on *a priori* partitioning equations. Misinterpreted experiments that did rely on such equations should be reinterpreted using strength CZM. Experiments would provide G_{tot} while strength CZM would vary normal and tangential strength models until predictions match experimental G_{tot}. If experiments can be fit, the modeling outputs would provide a revised partitioning of G_{tot} into G_I and G_{II}.

Instead of finding CZM energy release rate by Eq. (26), some might be tempted to evaluate J integral [38]. By choosing a contour surrounding all cohesive zones (both those in the

process zone and those with only elastic deformation), the J integral reduces to [23, 38, 39]:

$$J = \int_{\text{zones}} \boldsymbol{T} \cdot \frac{d\boldsymbol{u}}{dx} dx = J_I + J_{II} = \int_0^{u_n} dW_n + \int_0^{u_t} dW_t \tag{27}$$

where $dW_n = T_n du_n$ and $dW_t = T_t du_t$ are work increments evaluated for the debond-tip cohesive zone alone. This evaluation suggests that $J_I = \Omega_I$ and $J_{II} = \Omega_{II}$ where Ω_I and Ω_{II} are dissipated energies per unit area when the debond-tip cohesive zone fails. These J calculations are well defined and easily output as zones fail, but have two limitations. First, J integral only corresponds to energy release rate during self-similar crack propagation [38]. Because the mixed-mode propagation in Fig. 5 was non-self-similar, J differed from strength CZM energy release rates. Note that J integral was close to LEFM and only one curve is plotted because J was independent of σ_{nc}. A second J limitation is that the above evaluation only applies during decohesion. Thus J provides no information for evaluating zone-tip R curves that may partly occur while the debond tip is stationary.

Differences between CZM, LEFM, and J integral in Fig. 5 were caused by lack of self-similar propagation and influence of cohesive zone properties. Rice [38] has shown that if all point loads on the CBB specimen in Fig. 3 are replaced by pure moments, M_1 and M_2, on the two arms, the J integral can be evaluated independently of cohesive zone properties [38]. For a mid-plane crack, the fraction G_I for pure moment loading is [40]

$$\frac{G_I}{G_{tot}} = \frac{4(1-\phi)^2}{7-2\phi+7\phi^2} \quad \text{where} \quad -1 \le \phi = \frac{M_2}{M_1} \le 1 \tag{28}$$

This beam theory result is exact for pure moment loading (because shear corrections are not needed). Pure moment loading in mixed-mode testing has not been done, but one study did examine mode I delamination with moments applied by force couples on arm ends [41].

The next simulations compared CZM and J integral mode mixity to Eq. (28) for pure-moment loading. The moments were applied using force couples of increasing magnitude $F_i(t)$ separated by s on each arm for moments $M_i(t) = F_i(t)s$ (see Fig. 3). To keep moments valid after large arm rotations, the forces were set to remain normal to current arm ends. To prevent specimen rotation (whenever arm forces are unbalanced), the specimen's left edge was set to zero horizontal velocity and one point was set to zero vertical velocity. Simulations were run until the debond tip propagated 50 mm. Figure 6 plots strength CZM mode mixity as functions of debond-tip growth for G_I fractions 0, 25%, 50%, 75%, and 100% (by selecting $\phi = -1$, $1/3$, $7-4\sqrt{3}$, -1/5, and 1) for properties used above with $\sigma_{nc} = 2$ MPa. All CZM mode mixities were close to expected G_I/G_{tot} in Eq. (6) (dotted lines).

J integral calculations for pure mode I or II were correct, but mixed-mode J calculations started too high before approaching the expected result after about 10 mm of crack growth (see dashed curve in Fig. 6). Looking closer, J integral gave a constant and correct total energy released for all crack lengths because all crack growth was close to self similar. The errors for initial crack growth therefore implies that J does not partition into J_I and J_{II} as in Eq. (27) unless mode mixity remains constant. Here, mode mixity in these dynamic simulations varied for the first few cohesive zones, but became constant after some crack growth. As a result J

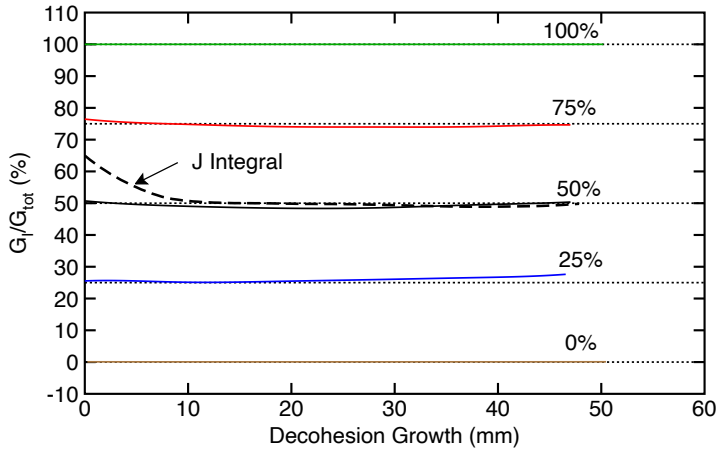

Figure 6: Mode mixity (% G_I) calculated by strength CZM as a function of debond-tip growth for CBB specimen in Fig. 3 when loaded by moments M_1 and M_2 on arm ends varied to get 0 to 100% G_I (solid lines). The dotted lines give expected mode mixity by Eq. (28). The dashed curve gives J integral calculation only for 50% G_I.

partitioning was invalid for the first cohesive zones, but then became valid after some crack growth.

In summary, R curves and mode mixity for materials with process zones modeled by CZM can be reliably calculated by differentiating total energy dissipated as a function of either zone-tip growth or debond-tip growth. J integral only applies to debond-tip growth and even then it is i) only valid during self-similar crack growth and ii) only partitions correctly for constant mode-mixity loading. The energy-differentiation methods are essential whenever process zone length or mode mixity might change.

3.4. Virtual Mixed Mode Experiments

The next simulations did virtual mixed-mode experiments using strength models in the previous section with $\sigma_{nc} = 2$ MPa and compared strength CZM to decoupled [13] and Högberg [16] methods. The fraction $v_I/(v_I + v_{II})$ was varied between 0 to 1 and simulations were run until initiation of debond-tip decohesion. The resulting values for G_I *vs.* G_{II} are cross plotted by the symbols in Fig. 7. As expected, the "Decoupled" model simply returned the imposed mixed mode failure criterion (which used $p = 1$ or $p = 2$ in Eq. (21)). The Högberg model was close to linear. Strength CZM gave a convex shape for G_I *vs.* G_{II} (*i.e.*, monotonically *increasing* signed slope or non-negative second derivative).

To see how strength models affect the shape, relative models were changed to $r_c = 0.05$ (which led to $\sigma_{tc} = \sigma_{nc}/8 = 0.25$ MPa). This significant change in relative properties had no effect on decoupled or Högberg simulations (results not plotted), but strength CZM methods changed shape. In other words, strength CZM can predict the role of relative normal and tangential strength models on mixed-mode failure properties.

If mode mixity remains constant (constant θ by Eq. (13)), which it did approximately up to onset of decohesion, CZM mixed-mode failure envelopes implied by various strength models can be found without numerical calculations. Integrating Eq. (11) from initial conditions to

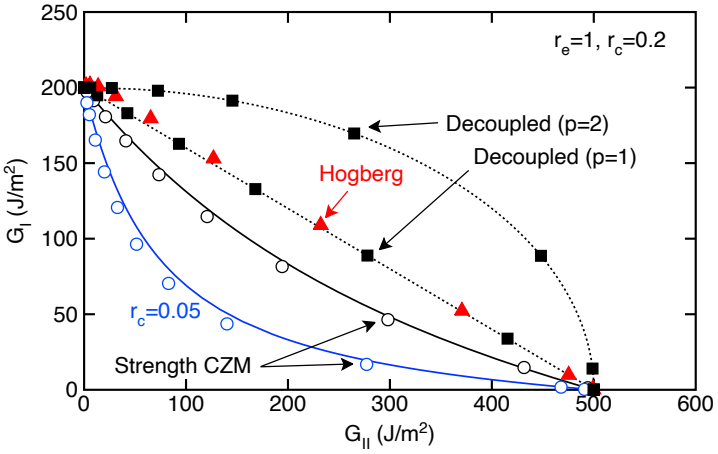

Figure 7: Predictions of mixed-mode failure envelopes using decoupled (squares), Högberg (triangles), and strength CZM (circles) approaches. All curves use $r_e = 1$ and $r_c = 0.2$ except the indicated strength CZM results used $r_c = 0.05$. Dotted curves are decoupled failure criterion for $p = 1$ or $p = 2$. The solid curves are strength CZM predictions using Eq. (30) for $r_c = 0.2$ and $r_c = 0.05$.

failure for constant θ, realizing that $\|\boldsymbol{u}\| \to \delta_d$ during damage evolution, and equating final energies to G_I and G_{II} gives:

$$G_I = \frac{1}{2}\int_{u_n^{(e)}}^{u_n^{(c)}} \frac{\varphi_n(\delta_n)\delta_n^2\delta_t^2\sin^2\theta}{\delta_t^2\sin^2\theta + \delta_n^2\cos^2\theta}d\delta_n \quad \text{and} \quad G_{II} = \frac{1}{2}\int_{u_t^{(e)}}^{u_t^{(c)}} \frac{\varphi_t(\delta_t)\delta_n^2\delta_t^2\cos^2\theta}{\delta_t^2\sin^2\theta + \delta_n^2\cos^2\theta}d\delta_t \tag{29}$$

When $D_n = D_t = D$, the δ variables are related by $\delta_t = D_t^{-1}\big(D_n(\delta_n)\big)$. These integrals cannot be evaluated in general, but, if normal and tangential strength models are both sawtooth laws and $r_e \neq r_c$, closed-formed integrations give:

$$\frac{G_I}{G_{Ic}} = \frac{\tan^{-1}(x) - \tan^{-1}(rx)}{(1-r)x}\tan\theta \quad \text{and} \quad \frac{G_{II}}{G_{IIc}} = rx^2\frac{G_I}{G_{Ic}} \tag{30}$$

where $r = r_c/r_e$ and $x = r_e\cot\theta$ varies from 0 (mode I) to ∞ (mode II). Limiting values as $x \to 0$ or ∞ are pure mode I or mode II results, respectively. The solid lines in Fig. 7 compare these predictions to strength CZM with $r_c = 0.2$ or $r_c = 0.05$. They agreed well.

For constant θ', similarly integrating the Högberg incremental energies in Eq. (24) for λ_ω from $\lambda_p(\theta')$ to 1 gives:

$$\frac{G_I}{G_{Ic}} = \sin^2\theta' = \frac{\sin^2\theta}{\sin^2\theta + r_c^2\cos^2\theta} = \frac{1}{1+r^2x^2} \quad \text{and} \quad \frac{G_{II}}{G_{IIc}} = \cos^2\theta' = 1 - \frac{G_I}{G_{Ic}} \tag{31}$$

which implies a linear G_I-G_{II} relation. The Högberg model (and by inference every effective-displacement model) is thus limited to modeling materials with linear mixed-mode failure envelopes. Because the simulations in Fig. 7 used $r_e \neq r_c$, Högberg calculations were invalid causing points to deviate slightly from linearity. When strength models use $r_e = r_c$, the δ

variables for sawtooth laws are related by $\delta_t = \delta_n / r_e$ and Eq. (29) reduces to a linear envelope. In other words, when the Högberg model is valid (*i.e.*, when $r_e = r_c$), it is a special case of strength CZM and both predict a linear failure envelope. But, if $r_e \neq r_c$, the Högberg model becomes invalid and remains close to linear, while strength CZM remains valid and can predict variations in failure envelopes caused by variations in normal and tangential strength properties.

To evaluate strength model effects, it is easy to show using the chain rule on Eq. (30) that $d^2 G_I / dG_{II}^2 \geq 0$ for all values of r and only equals 0 when $r = 1$. In other words, all G_I-G_{II} failure envelopes are predicted to be convex. The special case of $r = 1$ corresponds to a linear envelope. This observation includes strength models more ductile in shear than tension, or *vice versa*, and having more initial elastic deformation in shear than tension, or *vice versa*. To check other laws, numerical simulations were run using various trilinear or cubic laws in mode I or mode II. Again, all simulations had convex failure envelopes. If both directions are cubic laws, one can show that $\delta_t = \delta_n / r_c$ and the failure envelope follows the linear relation in Eq. (31).

3.5. Comparison to Experiments

The previous section showed that strength CZM unambiguously predicts G_I–G_{II} plots to be convex. Strength CZM is limited to these shapes because when normal and tangential damage parameters are connected, addition of mode II can either increase damage or cause no additional damage — it cannot reverse the damage. The question arises: are all experimental results convex? If the answer is yes, then elastic/damage strength CZM is a potential model that is consistent with experiments. If the answer is no, then either strength CZM is a poor model for the failure process or the experiments incorrectly partitioned total energy released into G_I and G_{II}.

First, consider composite delamination results that partitioned total energy release rate for failure, G_c, into G_I and G_{II} by methods that do not account for process zones. Johnson and Mangalgiri [36] used various mixed-mode carbon-fiber composite specimens with seven different resins and concluded all "appear" to have a linear G_I–G_{II} relation. Charalambides *et al.* [42] emphasized the importance of the method used to partition experimental results into G_I and G_{II}. Both their recommended partitioning and a proposed mixed-mode failure criterion gave convex G_I–G_{II} results. Reeder and Crews [3] developed the mixed-mode bending jig (MMB) to vary mode mixity without resorting to different specimen types. Their experimental results on carbon fiber/PEEK composites had a clear concave shape. Benzeggagh and Kenane [43] used the same MMB jig on E Glass/epoxy laminates and also found concave G_I–G_{II} curves. In a follow-up report, however, Reeder and Crews [37] showed that geometric non-linearities in the MMB jig caused initial results to be misinterpreted. They reanalyzed prior results with a nonlinear analysis and ran experiments using a new jig designed to minimize nonlinearities. Both these efforts resulted in carbon fiber/PEEK composites consistent with a linear G_I–G_{II} relation [37].

These cited experimental results suggest that many composites do have convex (which includes linear) G_I–G_{II} relations that are consistent with strength CZM analysis. As shown in section 3.3, however, any of those experiments that relied on *a priori* equations for partitioning

into G_I and G_{II} likely need to be repartitioned using strength CZM. A re-analysis is most crucial if the tested materials had non-negligible process zones lengths.

3.6. Crack Propagation and Precracking

Many fracture mechanics testing protocols recommend a precracking step with the goal being to induce a "natural" crack for subsequent propagation [20]. For materials with process zones, the goal of forming a natural crack raises two issues. First, the precracking phase may end before process zone development ends. Second, process zone development depends on precracking mode mixity. If precracking and testing mode mixities differ (which is common [3, 43, 44]), the testing phase will see an "unnatural" process zone that complicates interpretation of experiments. Indeed, experimental results for mode I toughness after precracking with different mode-mixities depend on both precracking methods and on the material (*e.g.*, cohesive zone properties) [44].

A final example evaluated precracking by simulating mode I crack propagation after mode II precracking. Beam and cohesive zone properties were the same as used above with $\sigma_{nc} =$ 2 MPa. Loading was applied by time dependent moments on arm ends. Mode II precracking was done with $M = M_1 = M_2$ ramped linearly to M_{pre} over time t_{pre} and then decreased linearly back to zero at $2t_{pre}$. M_{pre} was selected to induce process zone development but no decohesion. After $2t_{pre}$, the arms were loaded in mode I with $M = M_1 = -M_2$ ramped linearly until reaching self-similar crack propagation. Precracking and mode I loading used the same quasi-static loading rates (*i.e.*, sufficiently slow relative to arm vibration time). Simulation results were analyzed to find the debond-tip and zone-tip R curves.

Simulation of precracking effects using strength CZM, the Högberg approach, and the decoupled approach are given in Fig. 8. Because all methods are the same during pure mode II precracking, they all produced the same partial mode II process zone with length, $z_{pre} =$ 39 mm. This length was about half the fully-developed process zone when loaded in mode II to onset of decohesion. The three approaches differed dramatically in their subsequent mode I R curve predictions. Strength CZM appears most realistic and is explained as follows. The "natural" process zone for a pure mode I crack was $z_I = 8.5$ mm. As a result, when mode I loading encountered the much-larger, precracking process zone, it caused decohesion with debond tip propagation but no zone tip propagation. This new zone development continued until the process zone reverted to a natural mode I zone (*i.e.*, for crack growth of $\Delta a = z_{pre} - z_I = 30.5$ mm).

The debond-tip R curves (dashed lines in Fig. 8) and zone-tip R curves (solid lines in Fig. 8) were affected differently by precracking. Strength CZM gave a rising debond-tip R curve that plateaued at G_{Ic} after reaching self similar crack growth. Because the zone tip only propagated after reaching self-similar crack growth, the zone-tip R curve was flat and equal to G_{Ic}. The plotted zone-tip R curve stopped at about 10 mm of growth because that corresponds to end of the simulation at about 40 mm of debond tip growth. Both debond-tip and zone-tip R curves would continue flat if the simulations had continued to more propagation. The "Reference zone-tip R" curve in Fig. 8 is zone-tip R curve without precracking. Two differences caused by precracking are that the rising portion of the R curve depends on $z_{pre} - z_I$ instead of z_I and which crack tip causes that rise is reversed. Without precracking, a zone-tip R curve rises

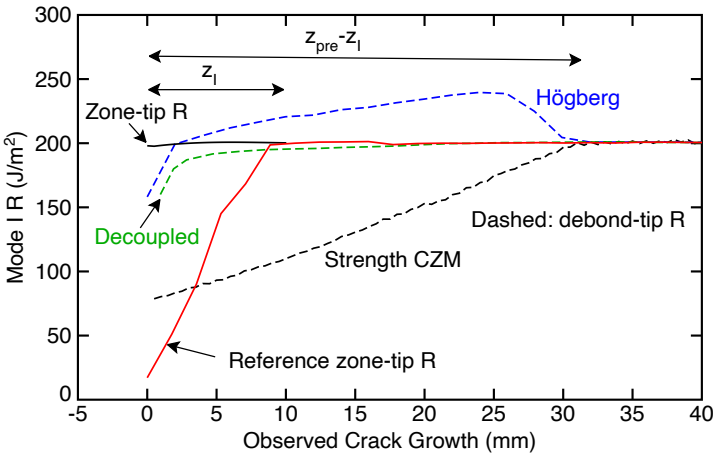

Figure 8: Mode I R curves after precracking in mode II that resulted in developing a process zone of length $z_{pre} = 39$ mm. The curves were predicted using decoupled, Högberg, and strength CZM approaches. Dashed lines are debond-tip R curves and solid lines are zone-tip R curves. The "Reference zone-tip R" is mode I, zone-tip R curve without precracking that developed a process zone of $z_I = 8.5$ mm.

while a debond-tip R curve is flat (see Fig. 4). With precracking, the opposite holds (at least whenever $z_{pre} > z_I$).

Simulations using decoupled CZM also had a rising region in the debond-tip R curve. The decoupled simulation in Fig. 8 used $p = 1.5$; the rising region expanded or shrank as p decreased or increased. This apparent coupling effect when using a decoupled model occurred because the simulation "remembered" mode II energy dissipation during precracking and that energy affected subsequent mode I failure by the imposed criterion in Eq. (21). One might expect that real materials would not remember prior dissipation, for example if mode I loading was done after the material had recovered from the precracking step. Alternatively, one might propose energy dissipation history as a viable approach to tracking damage state. Because such tracking defines damage states with altered decohesion properties but unaltered elastic properties, it may not be a realistic description of damage.

The Högberg results were unrealistically affected by precracking. Its debond-tip R curve rose above the mode I toughness and then returned to proper result after reaching self-similar crack growth. The problem with the Högberg approach is that these simulations, with $r_e \neq r_c$, were invalid because $\lambda_p(\theta')$ changed between mode II ($\theta' = 0$) precracking and subsequent mode I ($\theta' = \pi/2$) failure. The mode II precracking phase induced a process zone of the same $z_{pre} = 39$ mm. Within that zone, some cohesive zones reached damage states $\lambda_\omega > \lambda_p(0) = u_t^{(e)}/u_t^{(c)} = 0.04$. The energy to cause each pre-damaged zone to fail during the subsequent mode I phase calculated by integrating Eq. (24) from precracked λ_ω to 1 is:

$$\Omega_I = G_I = G_{Ic}\frac{1-\lambda_\omega}{1-\lambda_p(\pi/2)}$$

Because $\lambda_p(\theta')$ changed in mode I to $\lambda_p(\pi/2) = u_n^{(e)}/u_n^{(c)} = 0.2$, any cohesive zone precracked to $\lambda_\omega < \lambda_p(\pi/2)$, which was most of the process zone except near the debond tip, will report

erroneously high energy. A valid Högberg model (*i.e.*, laws limited to $r_e = r_c$) would have valid R values, but could only evaluate limited cohesive zone properties. In contrast, strength CZM provides new potential for evaluating precracking effects in fracture experiments.

4. Conclusions

A new coupled CZM method, labeled "strength CZM" and based on strength models rather than traction laws, is claimed to offer potential for improved simulations, especially for modeling mixed-mode failures. Strength CZM was derived using only three assumptions: 1. increments in damage occur when traction reaches a proposed failure envelope; 2. normal and tangential tractions simultaneously reach zero at failure; and 3. strength models correspond to monotonically decreasing effective stiffness. Numerical methods to adopt strength CZM require implementation of the updates in Eq. (16) (or numerical solution to Eq. (19)).

The development of process zones in CZM leads to the concept of two crack lengths defined by either zone-tip or debond-tip propagation. These two lengths imply two R curves — the zone-tip and debond-tip R curves — that must be calculated by differentiating total cohesive zone dissipated energy as a function of appropriate crack length.

Strength CZM of G_I-G_{II} failure envelopes predicts that all such envelopes are convex. While this prediction matches many experimental results, those experiments partitioned total energy into mode I and II using methods that ignore process zones. Because strength CZM shows that mode mixity depends on crack tip definition and differs significantly from calculations that ignore the process zone, any experiments that used that approach should be re-analyzed by coupling experiments to strength CZM calculations. Re-analysis examples are planned for future publications.

Prior methods based on effective displacements were identified as special cases of strength CZM when normal and tangential strength models are scaled copies of each other. Use of non-scaled laws in effective displacement models causes erroneous results. The problem with limiting CZM to scaled strength models is that it limits the modeling to materials with linear G_I-G_{II} envelopes. In contrast, strength CZM remains valid with non-scaled strength models. This feature gives strength CZM the potential to cover a wider variety of material properties and to realistically model problems with variable mode mixity, such as precracking methods.

Acknowledgement

This work was made possible by the endowment for the Richardson Chair in Wood Science and Forest Products.

Appendix A: Material Point Method Implementation

Strength CZM was fully implemented in the particle-based, material point method (MPM). The reader is referred to Ref. [23] for details on modeling cohesive laws in MPM. In brief, the implementation tasks are:

1. Create an MPM model with explicit cracks [31, 32]. Such cracks (in 2D) are discretized into a sequence of massless particles. As needed, crack particles can be assigned to a cohesive model with history variables initialized to $D = 0$, $\delta_n = u_n^{(e)}$, $\delta_t = u_t^{(e)}$, cumulative $\Omega_I = 0$ and $\Omega_{II} = 0$, and most recent $\boldsymbol{u} = (0, 0)$.

2. For time step m, calculate tractions on all crack particles based on input of updated displacement $\boldsymbol{u}^{(m)}$ or displacement increment $d\boldsymbol{u} = \boldsymbol{u}^{(m)} - \boldsymbol{u}^{(m-1)}$ (where latter is stored in particle history). When new tractions cause damage, use Eq. (16) to update D, δ_n, and δ_t and then use Eq. (11) to increment Ω_I, and Ω_{II} (if necessary, such as when $u_n^{(e)}$ is small, find dD by numerically solving Eq. (19) instead). If D reaches one, the particle is marked as failed by decohesion. The final tractions are transformed into forces by multiplying by crack area and rotating into global coordinates.

3. When crack surfaces are in contact, only the tangential traction is found using updates in Eq. (17) (which is valid for any $u_t^{(e)}$). The normal traction is determined instead using MPM crack-contact methods [31, 32], which eliminates the need to define compression response in the cohesive zone.

4. The standard MPM algorithm includes a task to extrapolate particle stresses to forces on the grid. When cohesive zones are present, this task also extrapolates cohesive zone forces calculated in step 2 to the grid.

Note that step 2 increments three damage variables, D, δ_n, and δ_n, but this model shows they are interrelated. Although tracking one is enough, numerical stability is enhanced by tracking all three and using the one explicit update in Eq. (16) that causes the smallest proportional change in its variable. The algorithm, which is based on comparing $d\delta_n/u_n^{(c)}$, $d\delta_t/u_t^{(c)}$, and dD, is: if $\max\left(\mathbb{R}_n u_n^{(c)}, \mathbb{R}_t u_t^{(c)}\right) < 1$, then update D; else if $\mathbb{R}_n u_n^{(c)} > \mathbb{R}_t u_t^{(c)}$, then update δ_n; else update δ_t. Once one variable is updated, calculate the other two by using or inverting Eq. (4). For typical strength models, this algorithm usually starts by updating δ_n or δ_t but then switches to updating D near decohesion.

Although cubic laws have $u^{(e)} = 0$, which normally requires numerical solution to Eq. (19), the special case of cubic laws for both normal and tangential directions satisfies the scaling requirements for an *effective* displacement approach. This special case can therefore be analyzed with $d\delta = u^{(c)} du_{\mathit{eff}}$ for each direction.

Appendix B: Finite Element Tangent Stiffness

Implementing strength CZM in FEA elements could use tangential stiffness matrices with damage state tracking. When using a single D parameter, the damage tensor simplifies to $\mathrm{diag}(D, D)$ and the tractions and the tangent stiffness become

$$\boldsymbol{T} = (1-D)\mathbf{K}\boldsymbol{u} \quad \Longrightarrow \quad d\boldsymbol{T} = (1-D)\mathbf{K}d\boldsymbol{u} - \mathbf{K}\boldsymbol{u}dD$$

For elastic increments, $dD = 0$ and the first term is linear elastic response using reduced normal and tangential stiffness. During damage evolution, substitution of dD in Eq. (16) and

elimination of $\mathbb{R}(\delta)$ terms provides the tangent stiffness:

$$\begin{pmatrix} dT_n \\ dT_t \end{pmatrix} = \frac{1}{\frac{k_n u_n^2}{\varphi_n \delta_n} + \frac{k_t u_t^2}{\varphi_t \delta_t}} \begin{pmatrix} \frac{S_n' k_n u_n^2}{\varphi_n} + \frac{S_n k_t u_t^2}{\varphi_t \delta_t} & -\frac{k_n u_n u_t}{\delta_t} \\ -\frac{k_t u_t u_n}{\delta_n} & \frac{S_t' k_t u_t^2}{\varphi_t} + \frac{S_t k_n u_n^2}{\varphi_n \delta_n} \end{pmatrix} \begin{pmatrix} du_n/\delta_n \\ du_t/\delta_t \end{pmatrix}$$

where S_i and φ_i implicitly depend on δ_i. For cohesive zones in contact, finite element analysis would either need to model element contact or implement a compression stiffness. Note that FEA implementation must also update damage parameters using Eq. (16). Because these updates depend on loading history, one cannot rely on simple equations or user-input tables for evolution of D; the explicit updates are essential.

Appendix C: Three Strength Models

This work allowed normal and tangential strength models derived from sawtooth, trilinear, or cubic cohesive laws. Implementation of any law only needs $S(\delta)$, $S'(\delta)$, and $\delta(D)$ (when needed, $D(\delta)$, $\varphi(\delta)$, and $\mathbb{R}(\delta)$ and are found from Eqs. (4) and (7)).

A sawtooth law rises linearly to $(u^{(e)}, \sigma_c)$ and decays linearly to $(u^{(c)}, 0)$. Its basic functions are:

$$S(\delta) = \frac{\sigma_c(u^{(c)} - \delta)}{u^{(c)} - u^{(e)}} \qquad S'(\delta) = \frac{-\sigma_c}{u^{(c)} - u^{(e)}} \qquad \delta(D) = \frac{u^{(e)} u^{(c)}}{u^{(c)} - D(u^{(c)} - u^{(e)})}$$

The initial stiffness is $k = \sigma_c / u^{(e)}$ and toughness is $G_c = (1/2)\sigma_c u^{(c)}$.

A trilinear law rises linearly to $(u^{(e)}, \sigma_c)$, changes linearly to $(u^{(2)}, \sigma_2)$, and then decays linearly to $(u^{(c)}, 0)$. Its basic functions are:

$$S(\delta) = \begin{cases} \frac{\sigma_c(u^{(2)} - \delta) + \sigma_2(\delta - u^{(e)})}{u^{(2)} - u^{(e)}} & u^{(e)} \le \delta \le u^{(2)} \\ \frac{\sigma_2(u^{(c)} - \delta)}{u^{(c)} - u^{(2)}} & u^{(2)} \le \delta \le u^{(c)} \end{cases} \qquad S'(\delta) = \begin{cases} \frac{\sigma_2 - \sigma_c}{u^{(2)} - u^{(e)}} & u^{(e)} \le \delta \le u^{(2)} \\ \frac{-\sigma_2}{u^{(c)} - u^{(2)}} & u^{(2)} \le \delta \le u^{(c)} \end{cases}$$

$$\delta(D) = \begin{cases} \frac{u^{(e)}(\sigma_c u^{(2)} - \sigma_2 u^{(e)})}{\sigma_c(1-D)u^{(2)} + u^{(e)}(D\sigma_c - \sigma_2)} & 0 \le D \le 1 - \frac{\sigma_2 u^{(e)}}{\sigma_c u^{(2)}} \\ \frac{u^{(e)} u^{(c)} \sigma_2}{\sigma_c(1-D)(u^{(c)} - u^{(2)}) + u^{(e)}\sigma_2} & 1 - \frac{\sigma_2 u^{(e)}}{\sigma_c u^{(2)}} \le D \le 1 \end{cases}$$

The initial stiffness is $k = \sigma_c / u^{(e)}$ and toughness is $G_c = (1/2)\big(\sigma_c u^{(2)} + \sigma_2(u^{(c)} - u^{(e)})\big)$.

A cubic law's peak is σ_c and both its value and derivative are zero at $u^{(c)}$. Its basic functions are:

$$S(\delta) = k u^{(c)} \overline{\delta} \left(1 - \overline{\delta}\right)^2 \qquad S'(\delta) = k\left(1 - \overline{\delta}\right)(1 - 3\overline{\delta}) \qquad \overline{\delta}(D) = 1 - \sqrt{1 - D}$$

where $\overline{\delta} = \delta / u^{(c)}$. This law has initial stiffness $k = 27\sigma_c/(4u^{(c)})$ and toughness $G_c = (9/16)\sigma_c u^{(c)}$. When a cubic law is used in Eq. (19), calculations for small D must switch to $\overline{\delta}(D) \to D/2$ to avoid round-off error causing $\overline{\delta}(D) \to 0$, even in double precision. Although a cubic law has $u^{(e)} = 0$, its peak is always located at $u = u^{(c)}/3$. Thus, all cubic laws are scaled copies of each other and could provide Högberg modeling [16] that is always valid by using $H(\lambda) = 27\lambda(1-\lambda)^2/4$.

References

[1] B. R. K. Blackman, H. Hadavinia, A. J. Kinloch, J. G. Williams, The use of a cohesive zone model to study the fracture of fibre composites and adhesively bonded joints, Int. J. Fract. 119 (2003) 25–46.

[2] B. F. Sorensen, Cohesive law and notch sensitivity of adhesive joints, Acta Mater 50 (2002) 1053–1061.

[3] J. R. Reeder, J. J. H. Crews, Mixed mode bending method for delamination testing, AIAA J. 28 (1990) 1270–1276.

[4] D. S. Dugdale, Yielding of steel sheets containing slits, J. Mech. Phys. Solids 8 (1960) 100–104.

[5] G. I. Barenblatt, The mathematical theory of equilibrium cracks in brittle fracture, Adv. Appl. Mech. 7 (1962) 55–129.

[6] V. Tvergaard, J. W. Hutchinson, Toughness of an interface along a thin ductile layer joining elastic solids, Philosophical Magazine A 70 (4) (1994) 641–656.

[7] L. Kachanov, Time of rupture process under creep conditions, Izv. Akad. Nauk SSR, Otd. Tekh. Nauk 8 (1958) 26–31.

[8] J. Chaboche, Le concept de contrainte effective appliqué à l'élasticité et à la viscoplasticité en présence d'un endommagement anisotrope, in: J.-P. Boehler (Ed.), Mechanical Behavior of Anisotropic Solids / Comportement Mécanique des Solides Anisotropes, Springer Netherlands, 1979, pp. 737–760.

[9] J. Oliver, Modelling strong discontinuties in solid mechanics via strain softening constitutive equations. Part 1: Fundamentals, International Journal for Numerical Methods in Engineering 39 (21) (1996) 3575–3600.

[10] J. A. Nairn, C. C. Hammerquist, Y. E. Aimene, Numerical implementation of anisotropic damage mechanics, Int. J. for Numerical Methods in Engineering 112 (12) (2017) 1846–1868.

[11] R. Dimitri, M. Trullo, L. D. Lorenzis, G. Zavarise, Coupled cohesive zone models for mixed-mode fracture: A comparative study, Engineering Fracture Mechanics 148 (145-179) (2015).

[12] Q. D. Yang, M. D. Thouless, Mixed-mode fracture analysis of plastically-deforming adhesive joints, International Journal of Fracture 110 (2) (2001) 175–187.

[13] S. Li, M. Thouless, A. Waas, J. Schroeder, P. Zavattieri, Mixed-mode cohesive-zone models for fracture of an adhesively bonded polymer–matrix composite, Engineering Fracture Mechanics 73 (1) (2006) 64 – 78.

[14] G. T. Camacho, M. Ortiz, Computational modelling of impact damage in brittle materials', Int. J. Solids Struct. 33 (1996) 2899–2938.

[15] P. P. Camanho, C. G. Dàvila, Mixed-mode decohesion finite elements for the simulation of delamination in composite materials, Tech. rep., NASA/TM-2002-211737 (2002).

[16] J. L. Högberg, Mixed mode cohesive law, International Journal of Fracture 141 (3) (2006) 549–559.

[17] A. Needleman, A continuum model for void nucleation by inclusion debonding, J. Appl. Mech. 54 (1987) 525–531.

[18] X. P. Xu, A. Needleman, Void nucleation by inclusion debonding in a crystal matrix, Modelling Simul. Mater. Sci. Eng 1 (1993) 111–132.

[19] M. Conroy, A. Kinloch, J. Williams, A. Ivankovic, Mixed mode partitioning of beam-like geometries: A damage dependent solution, Engineering Fracture Mechanics 149 (2015) 351–367.

[20] ASTM, Standard test method for linear-elastic plane-strain fracture toughness of metallic materials, ASTM Standards E399-20 (2020).

[21] J. G. Williams, Fracture Mechanics of Polymers, John Wiley & Sons, New York, 1984.

[22] M. Ortiz, A. Pandolfi, Finite-deformation irreversible cohesive elements for three-dimensional crack-propagation analysis, International Journal for Numerical Methods in Engineering 44 (9) (1999) 1267–1282.

[23] J. A. Nairn, Analytical and numerical modeling of R curves for cracks with bridging zones, Int. J. Fract. 155 (2009) 167–181.

[24] Abaqus Analysis User's Manual, Dassault Systèmes Simulia Corp., 2009, Ch. 29.5.6 Defining the constitutive response of cohesive elements using a traction-separation description.

[25] R. de Borst, J. J. C. Remmers, A. Needleman, Mesh-independent discrete numerical representations of cohesive zone models, Eng. Fract. Mech. 73 (2006) 160–177.

[26] M. J. van der Bosch, P. J. G. S. abnd M. G. D. Geers, An improved description of the exponential xu and needleman cohesive zone law for mixed-mode decohesion, Eng. Fract. Mech. 73 (2006) 1220–1234.

[27] N. Matsumoto, J. A. Nairn, The fracture toughness of medium density fiberboard (MDF) including the effects of fiber bridging and crack-plane interference, Eng. Fract. Mech. 78 (2009) 2748–2757.
[28] N. Matsumoto, J. A. Nairn, Fracture toughness of wood and wood composites during crack propagation, Wood and Fiber Science 44 (2) (2012) 121–133.
[29] B. Mirzaei, A. Sinha, J. A. Nairn, Measuring and modeling fiber bridging: Application to wood and wood composites exposed to moisture cycling, Comp Sci & Tech. 128 (2016) 65–74.
[30] E. Wilson, M. Shir Mohammadi, J. A. Nairn, Crack propagation fracture toughness of several wood species, Advances in Civil Engineering Materials 2 (1) (2013) 316–327.
[31] J. A. Nairn, Material point method calculations with explicit cracks, Computer Modeling in Engineering & Sciences 4 (2003) 649–664.
[32] Y. Guo, J. Nairn, Simulation of dynamic 3D crack propagation within the material point method, CMES - Computer Modeling in Engineering and Sciences 113 (4) (2017) 389–410.
[33] W. Goldsmith, Impact: The Theory and Physcial Behavior of Colliding Solids, Edward Arnikd Publishers, Ltd, London, UK, 1960.
[34] A. Carpinteri, Softening and snap-back instability in cohesive solids, Int. J. for Numerical Methods in Engineering 28 (1989) 1521–1527.
[35] J. A. Nairn, Generalized crack closure analysis for elements with arbitrarily-placed side nodes and consistent nodal forces, Int. J. Fracture 171 (2011) 11–22.
[36] W. S. Johnson, P. D. Mangalgiri, Influence of the resin on interlaminar mixed-mode fracture, Toughened Composites ASTM STP 937 (1987) 295–315.
[37] J. R. Reeder, J. J. H. Crews, Nonlinear analysis and redesign of the mixed-mode bending delamination test, NASA Technical Memorandum TM 102777 (1991).
[38] J. R. Rice, A path independent integral and the approximate analysis of strain concentration by notches and cracks, J. Applied Mech. June (1968) 379–386.
[39] G. Bao, Z. Suo, Remarks on crack-bridging concepts, Appl. Mech. Rev. 45 (6) (1992) 355–366.
[40] J. G. Williams, On the calculation of energy release rates for cracked laminates, Int. J. Fract. 36 (1988) 101–119.
[41] J. E. Lindhagen, L. A. Berglund, Application of bridging-law concepts to short-fibre composites part 1: DCB test procedures for bridging law and fracture energy, Comp. Sci. & Tech 60 (2000) 871–883.
[42] M. Charalambides, A. J. Kinloch, Y. Wang, J. G. Williams, On the analysis of mixed-mode failure, Int. J. Fract. 54 (1992) 269–291.
[43] M. L. Benzeggagh, M. Kenane, Measurement of mixed-mode delamination fracture toughness of unidirecitonal glass/epoxy composites with mixed mode bending apparatus, Comp. Sci. & Tech. 56 (1996) 439–449.
[44] P. Shankar, W. D. Bascom, J. A. Nairn, The effect of mixed mode precracking on the mode I fracture of composite laminates, in: Proc. of the 3^{rd} NASA Advanced Comp. Tech. Conf., Long Beach, CA, June 8-11, 1992.